UNIVERSITY of CALIFORNIA
Santa Barbara

LATTE:
A ground-based telescope for measuring the Milky Way Galaxy below 10GHz

A dissertation submitted in partial
satisfaction of the requirements for the
degree of Doctor of Philosophy
in Physics

by

Ishai Rubin

Committee in charge:

Professor Philip Lubin, Chair
Professor Peng Oh
Professor Ben Monreal

December 2014

The dissertation of Ishai Tov Rubin is approved.

Peng Oh

Ben Monreal

Philip Lubin, Committee Chair

September, 2014

LATTE:
A ground-based telescope for measuring the Milky Way Galaxy below 10GHz

by

Ishai Tov Rubin

Acknowledgments

September, 2014

I would like to thank my girlfriend Itzel for supporting me when I needed it most, my friend Josh for giving me an ear when I needed someone to bounce ideas around with, and my family for forgiving me for being a student for so long. I also owe a deep debt of gratitude to Peter Meinhold, for the invaluable experience and assistance he provides, and Phil Lubin for giving me the opportunity to make something happen, and the tools to do it with. I appreciate the generous contributions from the Ax Foundation, and Professor Brian Keating of UC San Diego, without whom this project would have never succeeded, and the California Space Grant Consortium for providing much needed support. I would also like to mention (in no particular order) Rory Barton-Grimley, Jon Suen, Connor Wolf, Brian Williams, Nate Stebor, Hugh O'Niel, Hamdi Mani, and all of the many students, graduate and undergrad, who contributed to this work.

VITA OF ISHAI TOV RUBIN

EDUCATION

Bachelor of Science in Physics, University of California, Santa Barbara, June 2005
Bachelor of Music in Piano Performance, University of California, Santa Barbara, June 2005
Master of Science in Physics, University of California, Santa Barbara, May 2012
Doctor of Philosophy in Physics, University of California, Santa Barbara, September 2014 (Expected)

PROFESSIONAL EMPLOYMENT

2007-2014: Teaching Assistant, Department of Physics, University of California, Santa Barbara
2007-2014: Graduate Student Researcher, Experimental Astrophysics, University of California, Santa Barbara

Abstract

LATTE: A ground-based telescope for measuring the Milky Way Galaxy below 10GHz

by

Ishai Tov Rubin

Advancements in CMB research have brought about not only a new age of precision cosmology, but also galactic astrophysics. WMAP has uncovered some tantalizing questions about the nature of dust emission in the galaxy, and has provided glimpses of a potentially new mechanism for energizing cosmic rays in the region around the center of the galaxy. The LATTE telescope has a single 9GHz receiver, Dicke switch radiometer operating at 30Hz, with a proven temperature uncertainty of under 10mK per switch cycle. The high sensitivity is due to a low noise cryogenic HEMT amplifier and a low loss cryogenic PIN diode switch. Using the optical design of the BEAST experiment, LATTE maps the microwave sky with an angular resolution of $\sim 1.5^{\circ}$ covering about half the sky in one 24 hour period. In this document the expected and actual performance are reviewed, and preliminary pseudo-maps are presented.

Contents

List of Figures

Chapter 1

Radio Sources

The radio sky is rich with interesting sources to study. Radio is the only part of the electromagnetic spectrum other than optical where the atmosphere is transparent enough to allow measurement of extraterrestrial sources from the ground. Without a large aperture, resolution limits the sources that can be measured, as radio wavelengths are so much longer than optical, even bright sources with very small angular size (such as stars and distant galaxies) are undetectable, or are spread out so much that they are unrecognizable (a phenomenon referred to as confusion). For relatively small radio telescopes in the millimeter or centimeter wavelength part of the radio spectrum, the measurable sources include the sun and moon, the planets, and diffuse emission from the Milky Way galaxy[1]

Diffuse galactic sources include thermal emission from (neutral) dust grains heated by the ambient ultra-violet radiation field from hot stars, thermal bremsstrahlung (or free-free) radiation from the interaction between ions and electrons, synchrotron radiation from relativistic cosmic ray electrons (accelerated by supernova shock fronts) interacting with the galactic magnetic field, and radiation from small spinning dust

[1]Other galaxies are certainly visible and interesting targets for telescopes with larger apertures and better angular resolution.

grains with nonzero electric dipole moments. There is also a synchrotron component near the center of the galaxy from electrons that appear to have a spectrum too hard to have been energized just by supernova shocks. Even the more well understood among these emission mechanisms have proven difficult to predict, and continue to pose a difficult obstacle for astrophysicists and cosmologists who wish to observe the diffuse radio source beyond the galaxy known as the microwave background.

1.1 Cosmic Microwave Background

The cosmic microwave background (CMB) dominates the sky temperature out of the galactic plane for frequencies between 30GHz and 150GHz [2]. It is a nearly perfect blackbody, with a temperature very close to 2.7K, corresponding to the temperature at which the first neutral atoms could form, red-shifted by a factor of over 1,000. The temperature anisotropies in the CMB inform the ΛCDM model and a host of other predictions about the physics of our universe.

In 2001 the WMAP instrument began the trip into orbit in the second Earth-Sun Lagrange point, with the goal of mapping the CMB with higher resolution and sensitivity than its predecessor, COBE. In addition to measuring a strong CMB signature, the 5 WMAP bands (at 23, 33, 40, 60, and 94GHz) gathered a wealth of information on the Milky Way galaxy. Part of the WMAP effort was to understand the galactic (foreground) signal well enough to remove it from the CMB map, but besides proving a challenging task, this effort has uncovered some interesting puzzles and questions about the physics of the inter-stellar medium (ISM). The WMAP CMB map is in figure 1.1.

Figure 1.1: The WMAP CMB Map

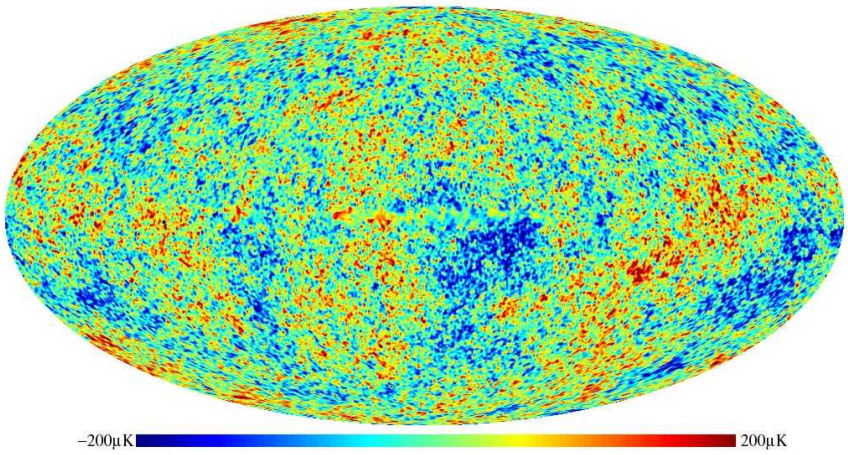

1.2 Galactic Foregrounds

Galactic foreground emissions are largely unexplored between 1.4GHz (Reich) and 23GHz (WMAP). Data at intermediate frequencies would improve the knowledge of well-understood sources and would help answer questions about those less understood sources. Well established components include thermal dust emission, synchrotron, and Free-free (Bremsstrahlung) emission. Sources that are still not well characterized in the data include radiation from small rotating grains (spinning dust), and the hard synchrotron near the galactic center from electrons energized by an unknown mechanism (haze).

Even one new map at an unexplored frequency would help to define the spectral index as it varies with position in the galaxy. It would help to clear up some long-standing questions about the nature and prevalence of non-thermal dust emission, and would provide another handle with which to grasp the haze. Maps at multiple frequencies would be even better (especially if they are taken with the same instrument) as they would provide more detailed spectral information.

Figure 1.2: The Finkbeiner Hα Map

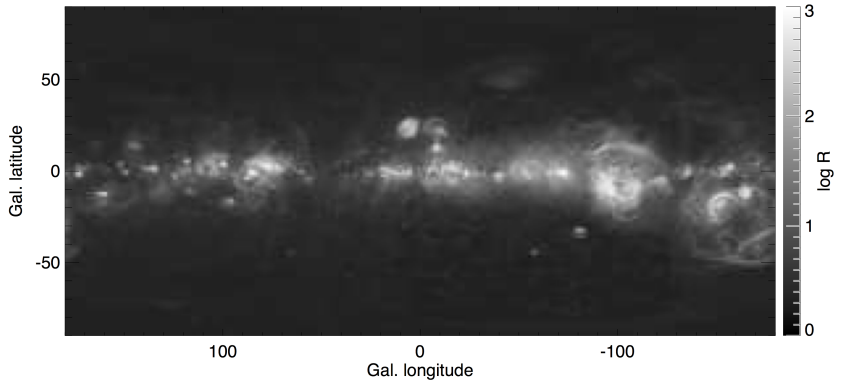

1.2.1 Free-free

Free-free (or thermal bremsstrahlung) radiation results from the acceleration of electrons in their interaction with ions in warm gas ($\sim$ 8000K). Emission is proportional to ionized gas density squared. This is because the collision rate is proportional to the ion density and the electron density, which are equal in an electrically neutral singly ionized gas.[2] Free-free emission follows a power law ($T \propto \nu^{\alpha}$) with spectral index $\beta \sim -2.51$ [14].[3]

Free-free doesn't dominate the spectrum at any frequency, so the best template available is Hα (wavelength 0.6563μm). Hα emission is also proportional to the square of the ionized gas density (and the emission measure) and can be used to trace free-free emission. An Hα map (figure 1.2) was assembled by Finkbeiner from several surveys including WHAM, VTSS and SHASSA [9]. The Hα template is limited in accuracy due to scattering and extinction by dust, but this can be corrected to some extent using the SFD dust map [4]. Since free-free emission depends on the actual gas temperature, this is also a source of uncertainty [2].

[2]Electron density squared, integrated along the line of sight is known as the emission measure.
[3]The temperature spectral index is commonly denoted by β, but this source listed it as α.

1.2.2 Thermal Dust

Interstellar dust clouds heated by UV radiation from core-collapse supernovae emit with spectral index related to grain size, composition and temperature. The thermal dust spectral index, which has an inverse relationship to temperature, is found to be $1.6 \leq \beta \leq 2.5$ suggesting emission from silicate grains that have a high spectral index at temperatures around 10K. Emission from dust at 16K is believed to come from carbon based grains [13].

Dust is mapped by WMAP at 94GHz and the FDS98 100μm and 240μm map. There is a strong correlation between the IR dust maps and synchrotron emission mapped by WMAP, thought to be due to the connection these two emission mechanisms have to star-forming regions [2].

1.2.3 Synchrotron

Synchrotron radiation is produced by relativistic cosmic ray electrons accelerated by core-collapse supernovae (type Ib and type II) interacting with galactic magnetic fields. The diffuse magnetic field strength is about 3 micro-gauss and thought to be related to supernovae activity. The radiation mechanism is non-thermal. When emitted from the relativistic electrons on curved paths through the galaxy, the radiation is beamed into a narrow angle that sweeps the observer in a short pulse. The duration of this pulse determines the observed frequency.[4]

The synchrotron spectral index in typical spiral galaxies is flattest (hardest), $\beta \sim -2.5$ near the star-forming regions of the galactic plane, and $\beta \sim -3$ in the halo[5]. The energy distribution in relativistic electrons goes as $N(E) \sim E^{\gamma}$ and the

[4]Synchrotron radiation can be up to 75 percent polarized, but with Faraday rotation its usually observed at less than 20 percent.

[5]The flux spectral index is expressed as $S \sim \nu^{\alpha}$, and the temperature index as $T \sim \nu^{\beta}$, with $\beta = \alpha - 2$ from the Rayleigh-Jeans law.

Figure 1.3: The Haslam 408MHz Map

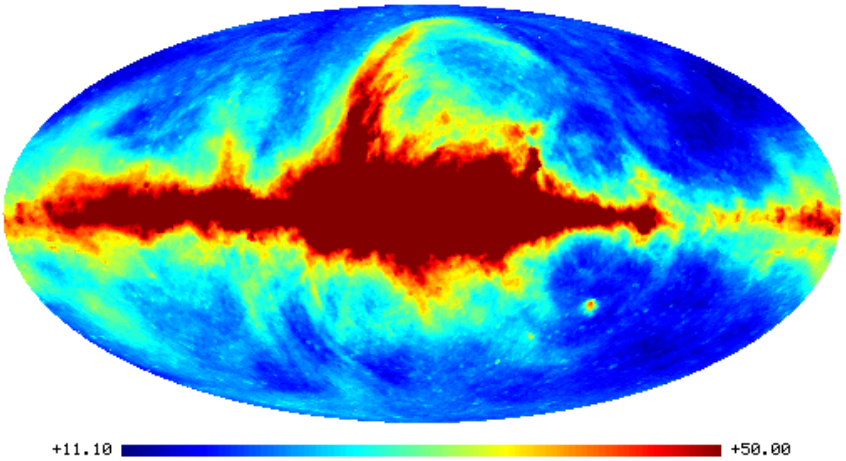

spectral index goes like $\alpha = -(\gamma - 1)/2$ above a few GHz, consistent with super-novae shock-front acceleration, diffusion in a leaky box and energy loss by inverse Compton scattering in the halo.[6]

Energy loss from self-absorption and free-free absorption becomes dominant at low-frequencies (a few MHz). At high frequencies, a break in the spectrum ($\Delta\beta \sim -0.5$) related to the age of the cosmic ray population is expected at 22GHz corresponding to a break at 20GeV in the electron energy spectrum.

Early studies at frequencies around 408MHz of the Haslam map (figure 1.3) found a spectral index of $\beta \sim -2.7$, and it was common practice to scale the Haslam data by this index. Comparing Haslam to the K-band WMAP, the spectral index is seen to vary from -3.4 in the halo to 2.3 in the plane demonstrating that the Haslam map is not a suitable tracer of the harder synchrotron components [2].

[6]In supernovae remnants the spectral index is close to $\beta \sim 2.5$ at a few GHz. The magnetic field around supernovae remnants is typically 75μG, whereas the diffuse galactic field varies from 1 to 5μG.

1.3 Anomalous Foregrounds

There are two emission mechanisms that are still not well established in the data. One of them is a dust correlated signal that does not follow a thermal dust spectrum. Depending on the dust composition and temperature the spinning dust spectrum peaks at 20GHz to 50GHz. This broad range of peaks has led to emission from this mechanism being overlooked and misidentified.

The other source that has yet to be fully understood is the so called haze. Finkbeiner [10] comments that a large free-free component uncorrelated to $H\alpha$ at temperature of $> 10^6$K would be required to explain the haze (once termed the free-free haze), but later concluded that these temperatures would be unstable. His other suggestion that the haze is due to a hard synchrotron component is the more likely explanation. The question then is what produces the cosmic ray spectrum for this hard synchrotron? The answer was postulated by Finkbeiner [11] and explored by Hooper, Finkbeiner and Dobler [3].

1.3.1 Spinning Dust

Spinning dust is believed to be the dominant emission mechanism between 10 and 30GHz. It is the result of charged dust grain, rotationally excited by a number of different mechanisms that emit at their rotation frequency. The composite spinning dust spectrum can have a spectral index $\beta \sim -2$ from 20 to 40GHz, with the upper limit determined by the fastest rotation rates. Emission from spinning dust would be relatively weak below a few GHz, but could easily be the dominant foreground mechanism at around 30GHz. Finkbeiner suggests that both high and low frequency roll off would need to be observed for a positive identification as spinning dust [6].

Given WMAP 94GHz dust emission, dust correlated 23 to 41GHz emission that

was higher than expected. Early work on this anomalous dust correlated component suggested it may be free-free or hard synchrotron. Kogut noticed emission that was well correlated with 250um dust but not with 480MHz synchrotron. The dust correlated signals were brighter at 31GHz than 53GHz with an index $\beta \sim -2.2$ very close to that of free-free. Oliveira De Costa, in her work on the Saskatoon data also identified the anomalous emission as free-free, since it was correlated with with IR dust, but not with synchrotron.

The superposition of spectra from spinning dust at different temperatures and composition makes the total spinning dust spectrum resemble a hard synchrotron component. Data studied by Leicht at 14.7 and 31.7GHz found emission described by a single index of $\beta \sim -2.1$, but given null data at 325MHz for the same region ruled out synchrotron. Free-free was also found unlikely due to the absence of Ha emission in that region.

WMAP 22 to 33GHz data also shows a dominant emission with a synchrotron-like spectrum but dust-like spacial morphology. In the spinning dust model of Draine and Lazarian [1], the warm ionized medium (WIM at 8000K) emission peaks at 40GHz and the cold neutral medium (CNM at 100K) emission peaks between 20 and 30GHz. The latter was thought to be present in WMAP since the spectrum falls from 23 to 41GHz, but it was suggested that high-quality diffuse maps between 5 and 15GHz were needed to be sure [13].

The work of Dobler and Finkbeiner has made a strong case for spinning dust, by using template subtraction methods specifically designed to find anomalous emission. They used the 3-year WMAP data to find a 20 percent bump at 50GHz in the WMAP data, but in their 2008 paper based on the 5-year WMAP data, using Hα to trace for free-free and WIM, found that the subtracted spectrum of spinning dust (not correlated with thermal dust) peaks at 40GHz, with about a third the amplitude

Figure 1.4: The WIM Bump and CNM Rise

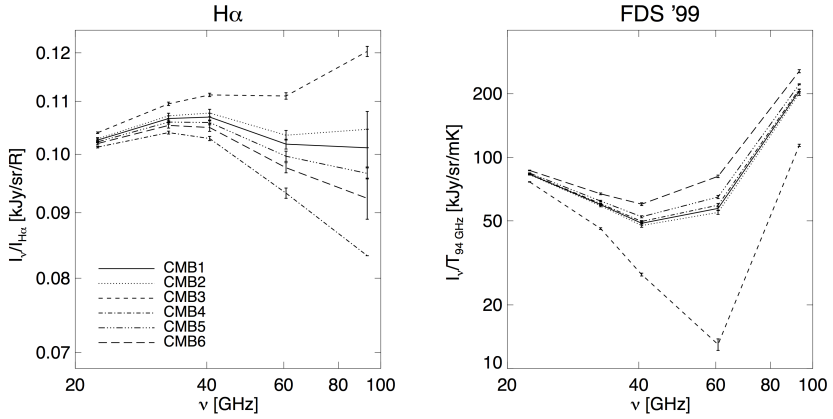

predicted by the Draine Lazarian model. A strong indication that their findings are not wrong is that regions thought to be free-free dominated show residual emission when WMAP K-band scaled with a free-free spectrum is subtracted, which should over-subtract free-free. Using the FDS98 dust template for the CNM, the subtracted spectrum falls from 23-60GHz (figure 1.4), suggesting that data at frequencies below those WMAP are needed to identify a CNM spinning dust component. Part of the difficulty in identifying spinning dust is that along any line of sight there may be a combination of these two types of spinning dust [14].

1.3.2 WMAP Haze

The WMAP haze, an amorphous excess emission near the galactic center, is still a real mystery. Finkbeiner thought it could be free-free [10], but this would require gas temperatures 10^5K, which would be thermally unstable in the ISM. He later turned to dark matter as a possible explanation for the emission [11].

Dobler and Finbeiner used similar subtraction methods to those used to identify spinning dust in their search for the haze. Using fixed templates, the Finkbeiner Hα map, the Schlegel 94GHz dust map, which also traces spinning dust, and Haslam to

Figure 1.5: The Haze

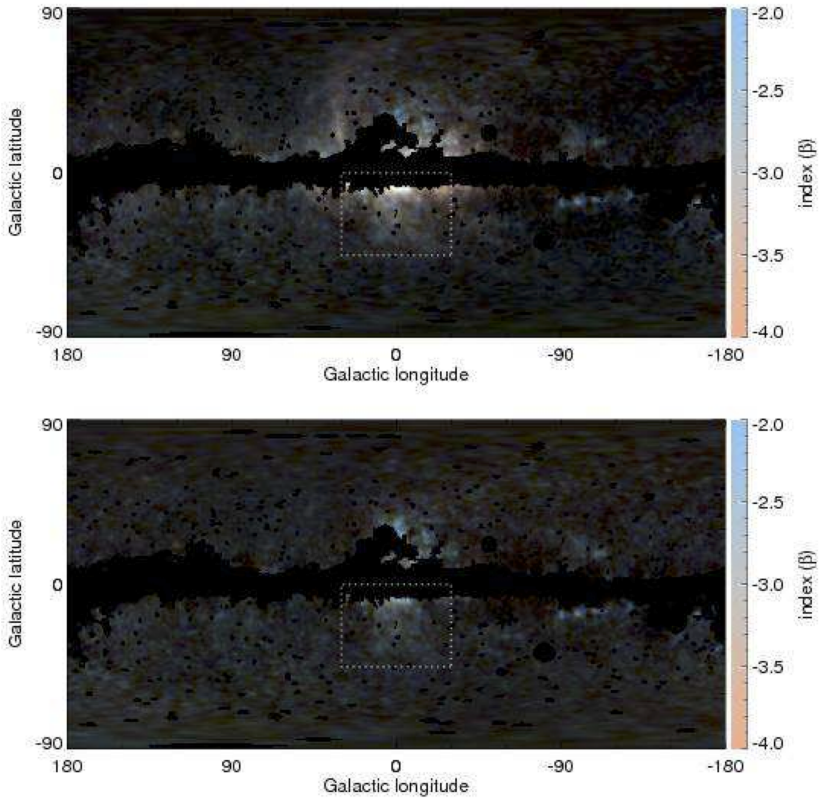

trace soft synchrotron, along with several CMB estimators, and studying residuals left after subtraction they show the existence of a haze for multiple CMB estimators from the WMAP data, suggesting that the haze is not an artifact from the CMB estimator (figure 1.5). They conclude that the best explanation is hard synchrotron with spectral index of $\beta \sim -2.5$, morphologically different from soft synchrotron.

Since the haze spectrum does depend on CMB estimator, the new Plank data should help with better CMB estimators [14]. Even with the improvement better CMB data will provide at high frequencies, data at frequencies lower that those of WMAP would expect to see a large haze component, and could provide new information about the haze spectrum and morphology.

Figure 1.6: The Full Sky PSM at 8GHz

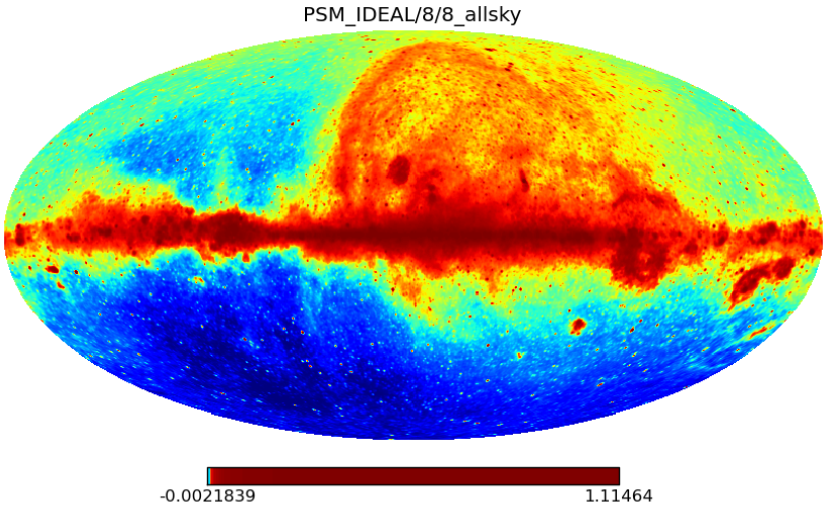

1.4 Plank Sky Model

As part of the European Space Agency program to launch the Plank satellite, a model was developed in an attempt to predict to a high degree, the emission that could be expected. This model, the Plank Sky Model (PSM) extends to frequencies well below WMAP, and can help inform expectations for lower frequency instruments.

In figure 1.6 is the full sky PSM evaluated at 8GHz. The full sky simulation includes all of the components expected to contribute to the antenna temperature. The antenna temperature appears to peak at about 1K in the plane of the galaxy.[7]

[7]The temperature scale is not balanced in the plot, so temperatures other than the peak are difficult to estimate.

Chapter 2

Noise

The study of noise is central to radio astronomy not only because astronomers are always pushing the limits of sensitivity but because many of the signals being measured are themselves noise. Thermal noise is present in all radio measurements and it is often convenient to express receiver outputs in Kelvin, with reference to blackbody sources or warm resistors of equivalent temperature.[1]

2.1 Blackbody Radiation

Blackbody radiation is produced by sources having non-zero opacity and reflectivity less than unity, at nonzero temperatures. It is described by Planck's law, which gives the spectral brightness B_ν in power per unit receiver bandwidth, per unit area of the antenna, per steradian of solid angle subtended by the source.

$$B_\nu(T) = \frac{2h\nu^3}{c^2} \frac{1}{\exp(\frac{h\nu}{kT}) - 1} \tag{2.1}$$

For reference:

[1]Thermal noise is universal in that it is produced by all matter.

- Planck's constant h, is $6.63 \times 10^{-27}\text{erg} \cdot \text{s} = 6.63 \times 10^{-34}\text{J} \cdot \text{s}$.
- Boltzmann's constant k, is $1.38 \times 10^{-16}\text{erg} \cdot \text{K}^{-1} = 1.38 \times 10^{-23}\text{J} \cdot \text{K}^{-1}$.
- The speed of light c, is $3 \times 10^{10}\text{cm} \cdot \text{s}^{-1} = 3 \times 10^{8}\text{m} \cdot \text{s}^{-1}$.
- ν is the frequency in Hertz.
- T is the temperature in Kelvin.

Plank's law can be obtained from the energy density of standing wave modes in a blackbody cavity[2],

$$u_\nu = 8\pi \frac{\nu^2}{c^3} \langle E \rangle, \tag{2.2}$$

which depends the average energy per mode[3] given by a Boltzmann distribution with quantized photon energies.

$$\langle E \rangle = \frac{h\nu}{\exp(\frac{h\nu}{kT}) - 1} \tag{2.3}$$

In the Rayleigh-Jeans limit,[4] when $h\nu \ll kT$, it is safe to make the classical approximation that all of the modes have the same average energy $\langle E \rangle \approx kT$ leading to the Rayleigh-Jeans law:

$$B_\nu(T) = \frac{2kT\nu^2}{c^2} \tag{2.4}$$

[2]The blackbody cavity must have physical dimension $a \gg \lambda$.

[3]See appendix on average energy and geometric series.

[4]For an object at room temperature ($T = 300\text{K}$) at around 10GHz, $\frac{h\nu}{kT} = \frac{6.63\times10^{-27}\text{erg}\cdot\text{s}\times10^{10}\text{Hz}}{1.38\times10^{-16}\text{erg}\cdot\text{K}^{-1}\times300\text{K}} \approx 1.6 \times 10^{-3}$, and the spectral power has a relative error of 8×10^{-4}.

2.2 Johnson Noise

Johnson-Nyquist noise is the one dimensional version of blackbody radiation. In the Rayleigh-Jeans limit the energy density of standing wave modes on a transmission line connecting two matched resistors is independent of frequency:

$$u_\nu = \frac{2}{v}\langle E \rangle = \frac{2}{v} kT \tag{2.5}$$

where v is the propagation velocity. The power per unit frequency produced by two resistors is $P_\nu = 2kT$, so for a single resistor[5]

$$P_\nu = kT. \tag{2.6}$$

If the resistor at one end of the transmission line is replaced by an ideal antenna at equilibrium inside of a blackbody cavity at the same temperature as the resistor, thermodynamics demands that the spectral power received by the antenna must equal that from the resistor at the other end of the transmission line.[6] In this way a matched resistor on a transmission line is essentially a one dimensional blackbody, and is indistinguishable from an antenna observing a blackbody radiator at the same temperature. This makes resistors useful for calibrating receivers.

Johnson noise, as the name suggests, can also be an undesirable component of receiver noise. If it is due to resistive elements in the receiver itself, and not a target under measurement, it will reduce the overall sensitivity.

[5]The total noise power from a 300K source in a 1GHz wide band is $P = 4.14 \times 10^{-12}$W, about 4 picoWatts.

[6]If the power from one side was greater than the power from the other, the temperature would rise on one side and fall on the other, which would violate the second law of thermodynamics.

2.3 Uncertainty and Sensitivity

Johnson-Nyquist noise is often described by the RMS voltage, or standard deviation of the voltage, per unit bandwidth (from two resistors):

$$v_\nu = \sqrt{4kTR}. \tag{2.7}$$

This voltage noise has the two properties of a wide-sense stationary (WSS) signal; it has a constant mean and the covariance, defined below, depends only on the time difference or time lag $t_1 - t_2 = \tau$ [19, p. 22]. It also has the properties of Gaussian white noise since it has a constant mean of zero, a constant power spectral density (PSD)[7] and a standard normal distribution. For a given sample of voltage noise, the sample variance per unit bandwidth (the square of the sample standard deviation) is proportional to the spectral power in that sample.[8] The sample variance (often denoted s^2 to distinguish it from the population variance, σ^2) is itself a random variable and has a variance[9]

$$V[s^2] = \frac{2\sigma^4}{N-1}, \tag{2.8}$$

where N is the number of independent measurements of the signal and σ^2 is proportional to the actual temperature.[10] So, how many times does the receiver make an independent measurement of the signal? The receiver actually measures an average

[7] As mentioned above the power per unit bandwidth is not actually constant to arbitrarily high frequencies.

[8] Electrical power is $\frac{V^2}{R}$ and since each resistor is responsible for only half of the voltage, the power is $\frac{v_\nu^2}{4R} = kT$ as above.

[9] This comes from Bessel's correction in the unbiased estimation of standard deviation, and the variance of the χ^2 distribution, the distribution of the sum of the squares of independent standard normal variables.

[10] Population variance is proportional to the true spectral power, $P_\nu = kT$, which is proportional to the actual temperature.

of the continuous signal, so a more meaningful question is how many independent pieces of information are available to the receiver during a measurement? The answer to this question depends on the radiometer.

A total power radiometer measures the noise power in an RF band, usually determined by a band-pass filter. After passing through the filter the signal can no longer be described as white noise because it only has frequency components in a limited range. Instead it can be thought of as a baseband (with frequency components down to DC) band-limited white noise signal that has been modulated (multiplied) by a carrier frequency equal to the lowest frequency in the band-pass filter range $f_c = \frac{\omega_c}{2\pi}$.[11] The filter output is sent to a detector diode to rectify the signal and a low pass filter that smooths over high frequency oscillations. The output of a detector with a linear voltage response (sometimes called an envelope detector) is the amplitude or the envelope of the signal. The highest frequency components in the base-band output are $\omega_m = 2\pi f_m$, where f_m is the filter bandwidth in Hertz.

The power out of the RF section of the receiver is on the order of microWatts, which is low enough to allow the diode to operate in the square-law regime. The square law detector diode not only rectifies the signal, but also squares it, which changes the frequency domain characteristics.

The Fourier transform of the product of two time-domain function, $x(t)$ and $y(t)$ is the convolution of the Fourier transforms ($X(\omega)$ and $Y(\omega)$) of those function. The convolution of two frequency domain functions is

$$\{X * Y\}(\omega) = \int_{-\infty}^{\infty} X(w)Y(w-\omega)\mathrm{d}w. \tag{2.9}$$

The Fourier transform of the square of a time-domain function is the convolution

[11] This would have to be single-sideband (SSB) modulation.

of the Fourier transform of the function with itself (equivalent to the autocorrelation). This convolution has a baseband triangle function component that is maximum at $\omega = 0$ and goes to zero at $|\omega| = \omega_m$. It also has a copy of base-band triangle centered on $\omega = 2\omega_c + \omega_m$ from the overlap of the original band and its negative frequency copy (at $\pm(\omega_c + \frac{\omega_m}{2})$ respectively). This higher frequency component can be ignored since it is smoothed away by the low pass filter.

The output of the total power radiometer can be understood by considering the power spectral density. First consider the demodulated signal without squaring. Following Porat [19], band-limited white noise has a rectangular function PSD denoted by K,

$$K(\omega) = \begin{cases} kT, & |\omega| < \omega_m \\ 0.5kT, & |\omega| = \omega_m \\ 0, & |\omega| > \omega_m \end{cases}$$

The PSD is defined as the Fourier transform of the (auto)covariance $\kappa(\tau)$ of a WSS signal[12]

$$K(\omega) = \int_{-\infty}^{\infty} \kappa(\tau) \mathrm{e}^{-i\omega\tau} \mathrm{d}\tau, \tag{2.10}$$

where the autocovariance is defined as

$$\kappa_x(\tau) = E\left[x(t+\tau)x(t)\right].^{13} \tag{2.11}$$

The inverse transform is

[12] According to the Wiener-Khinchin theorem.

[13] The covariance is symmetric; $\kappa_x(\tau) = \kappa_x(-\tau)$.

$$\kappa(\tau) = \frac{1}{2\pi}\int_{-\infty}^{\infty} K(\omega)\mathrm{e}^{i\omega\tau}\mathrm{d}\omega, \tag{2.12}$$

where τ is the time difference or lag time between two samples. The inverse transform of a band limited white noise spectrum is a sinc function

$$\kappa(\tau) = \frac{1}{2\pi}\int_{-\omega}^{\omega} kT\mathrm{e}^{i\omega\tau}\mathrm{d}\omega = \frac{1}{2\pi}\frac{kT}{i\tau}\left(\mathrm{e}^{i\omega_m\tau} - \mathrm{e}^{-i\omega_m\tau}\right) = \frac{kT\omega_m}{\pi}\mathrm{sinc}\left(\frac{\omega_m\tau}{\pi}\right), \tag{2.13}$$

The normalized sinc function is defined in Porat[19, p. 16] as follows.

$$\mathrm{sinc}(t) = \begin{cases} \frac{\sin(\pi t)}{\pi t}, & t \neq 0 \\ 1, & t = 0 \end{cases}$$

The maximum of the covariance function at $\tau = 0$ is equal to the variance $kT\omega_m/\pi$ (which is proportional to the total power in bandwidth $f_m = \frac{\omega_m}{2\pi}$ from a resistor at temperature T).The correlation is zero for values of τ separated by exactly $\tau = 1/(2f_m)$, so on average, the product of the signal at times t and $t + \tau$ is zero for $\tau = 1/(2f_m)$.

The autocorrelation of a sinc function turns out to also be a sinc function of the same frequency, so the signal itself is a sinc function and the output of the radiometer (including the square law detector) is a sinc^2 (the inverse Fourier transform of a triangle function in frequency is also sinc^2).

This would suggest that the signal is a sinc^2 pulse of width $1/(f_m)$ centered on some unknown (random) time (since the auto-covariance is independent of t), but we know that the signal is continuous so as the ERA chapter on radiometers suggests, the pulses repeat at random, and on time-scales of $1/f_m$.

There is on average 1 pulse every period, and we might conclude that each pulse

is one piece of information (an independent measurement, with its own error) so the information rate is f_m, but this would be incorrect. From a sampling standpoint, if the pulses were measured at exactly the peak every time the measurement would provide the maximum amplitude, which would be proportional to the power. But if instead the measurements take place at random points along the pulse, sometimes the amplitude would be zero providing no information at all about that peak, but in general the amplitude would be random and it would take many such measurements to provide an average. The answer is instead to sample at (at least) twice the pulse frequency ($f_s = 2f_m$) so that the amplitude of each pulse can be determined. Sampling at higher rates does not provide more information.[14]

The rate at which information is available is the same as the minimum sampling rate needed to insure no loss of information. The sampling theorem provides an analytic explanation for the minimum sampling rate of $2f_m$ (also known as the Nyquist rate) by relating the Fourier transform of a discrete-time (or point sampled) signal $X^f(\theta)$ to that of the continuous sampled signal X^F. Again using Porat's notation:

$$X^f(\theta) = \frac{1}{T} \sum_{k=-\infty}^{\infty} X^F \left(\frac{\theta - 2\pi k}{T} \right) \tag{2.14}$$

and the PSD of a point sampled WSS signal is (Eq. 3.59 in Porat)

$$K_x^f(\theta) = \frac{1}{T} \sum_{k=-\infty}^{\infty} K^F \left(\frac{\theta - 2\pi k}{T} \right) \tag{2.15}$$

Here $\theta = \omega T$, sometimes called normalized frequency, is the discrete-time frequency and T is the sample period. The sampling theorem says that the Fourier transform of a discrete-time signal is the sum of an infinite number of copies of the Fourier

[14]Since the period is know, fitting the pulse function requires only two samples taken at known times.

transform of the continuous-time signal X^F separated by $2\pi/T = \omega_m$. A band-limited signal with Fourier transform of zero above f_m, when sampled at a rate $f_s \geq 2f_m$, will have a Fourier transform where the copies of X^F do not overlap. This is important for reconstruction of the signal. If the copies overlap, they become distorted and cannot be used to reproduce the original signal. The changes to the signal due to this overlap in the Fourier transform is called aliasing.

Since the minimum number of samples per second needed to reproduce the signal without distortion is $2f_m$ it appears that the number of independent measurements that are available to the radiometer are $2f_m t$, for time (t) in seconds. If $2f_m t$ is a large number (bandwidths of total-power radiometers range from a few MHz to a few GHz), we can approximate $(N-1) \approx N$ in the expression for the variance of the sample variance, and the standard deviation of the sample variance becomes

$$\sigma[s^2] = \sqrt{\frac{2\sigma^4}{N}}. \tag{2.16}$$

Recall that the true temperature is proportional to the population variance (per unit bandwidth) of the measured voltage

$$T = \frac{P_\nu}{k} = \frac{v_\nu^2}{4Rk}, \tag{2.17}$$

and use the property of the standard deviation,

$$|a|\sigma(x) = \sigma(ax), \tag{2.18}$$

to show that the standard deviation of the sample variance of the noise voltage, $s_{v_\nu}^2$ is proportional to the standard deviation (or uncertainty) of the measured temperature in terms of the true temperature, σ_T.

$$\frac{1}{4Rk}\sigma[s^2_{v_\nu}] = \frac{1}{4Rk}\sqrt{\frac{2v_\nu^4}{N}} = \sqrt{\frac{2T^2}{N}} = \sigma_T \tag{2.19}$$

Plugging in $N = 2f_m t$, we get the radiometer equation:

$$\sigma_T = \frac{T}{\sqrt{f_m t}} \tag{2.20}$$

The radiometer equation gives the uncertainty in a measurement of the temperature of a thermal noise source in terms of the true temperature T, the measurement bandwidth f_m and the measurement time t. For example, a thermal source of temperature 10K measured over a 1GHz band for 1 second would have an uncertainty of just over 300μK and a relative error of about 3×10^{-5}. The sensitivity is usually taken to be 5 times the uncertainty, so for this measurement the radiometer has a sensitivity of about 1.5mK, which is to say that a temperature difference as small as 1.5mK could be detected.

2.4 The Quantum Limit

An amplifier-based total power receiver is called a coherent detector because it preserves the phase information of the signal. This means that the measurement uncertainty of a signal of arbitrarily small temperature can be determined by the quantum uncertainty principle

$$\Delta E \Delta t \geq \frac{h}{2}, \tag{2.21}$$

where h is planks constant, ΔE is the energy uncertainty and Δt is the uncertainty in the time. Writing the energy in terms of the number of photons $n = E/h\nu$ and the time in terms of the phase $\phi = 2\pi\nu t$, this can be re-written as

$$h\nu\Delta n\frac{\Delta\phi}{2\pi\nu} \geq \frac{h}{2}, \tag{2.22}$$

or,

$$\Delta n\Delta\phi \geq \pi. \tag{2.23}$$

The approximation for the energy per blackbody mode $\langle E\rangle \approx kT$ can be used to relate the number of photons to the temperature,

$$h\nu\Delta n = k\Delta T, \tag{2.24}$$

and the time interval between independent measurements provided by the sampling theorem, $\Delta t = 1/2\nu$, can be used to find that $\Delta\phi = \pi$. The result is

$$\Delta T \geq \frac{h\nu}{k}. \tag{2.25}$$

The quantum limited temperature uncertainty is determined only by the frequency. At 10GHz this uncertainty is 0.48K. This is the minimum uncertainty for a single measurement of a source, even if the source temperature is less than 0.48K. Plugging this temperature into the radiometer equation gives the shot noise for a measurement of a thermal source over a bandwidth f_m for time t.[15].

$$\sigma_{T,q} = \frac{\Delta T}{\sqrt{f_m t}} \tag{2.26}$$

[15]This is the uncertainty in the temperature due to the uncertainty in the number of photons per unit time arriving at the receiver.

2.5 Calibration

The radiometer measures temperature but the output of the baseband electronics is a voltage V_{dc} that is proportional to the detector diode output voltage plus an offset V_0.[16] Following the notation used by Gaier [20] the baseband gain is G_{dc}[17], and the baseband output voltage is

$$V_{dc} = G_{dc}(V_d + V_0). \tag{2.27}$$

The diode output voltage is itself proportional to the thermal noise power out of the RF section of the radiometer,

$$V_d = KGkT_{sys}f_m, \tag{2.28}$$

where K is the detector diode response coefficient in $[\mathrm{V} \cdot \mathrm{W}^{-1}]$, G is the total RF gain, T_{sys} is the total system temperature and f_m is the RF bandwidth. The radiometer output is then

$$V_{dc} = G_{dc}(KGkT_{sys}f_m + V_0). \tag{2.29}$$

If the voltage offset is known, the radiometer output voltage can be related to the noise temperature at the receiver input (usually called the antenna temperature, T_A) by calibrating with a thermal load of known temperature (such as a resistor or a blackbody that fills the antenna beam). For real radiometers, calibration cannot be done with just one reference load because the total (system) noise temperature is due not only to the thermal load, but also to noise from the receiver itself.[18]

[16] There is also a small noise component from the op-amp that is ignored here. See pre-amp section.

[17] Wollack [7] calls this video gain G_{video}.

[18] There are two sources of noise in the receiver: thermal noise generated in the amplifier circuits,

$$T_{sys} = T_L + T_{rec} \tag{2.30}$$

The receiver temperature is independent of the input temperature (T_L) and can be determined by taking two calibration measurements at two different temperatures. For best results, one reference is at a relatively high temperature T_h and one at an intermediate or cool temperature T_c.

Assuming the radiometer response is linear[19] we have

$$V_h = G'(T_h + T_{rec}) \tag{2.31}$$

and

$$V_c = G'(T_c + T_{rec}) \tag{2.32}$$

where $V_h = \frac{V_{dc_h}}{G_{dc}} - V_0$ is the average voltage out of the diode and $G' = kKGf_m$ is the effective receiver gain. This gives

$$T_{rec} = \frac{T_h - YT_c}{Y - 1} \tag{2.33}$$

where $Y = \frac{V_h}{V_c}$. This method of determining the system temperature is called the y-factor method.

The relative uncertainty in the measurement of the system temperature for a calibration time t_c is

$$\frac{\sigma[T_{sys}]}{T_{sys}} = \frac{1}{\sqrt{f_m t_c}}, \tag{2.34}$$

and gray-body radiation from lossy elements in the receiver chain (see receiver section).

[19] A system with linear response has gain G and diode coefficient that are constant over the range of power being measured.

so the y-factor will have a relative uncertainty of

$$\frac{\sigma_Y}{Y} = \sqrt{\frac{2}{f_m t_c}}, \tag{2.35}$$

and the derived receiver temperature will have a relative uncertainty of

$$\frac{\sigma[T_{rec}]}{T_{rec}} = \frac{2}{\sqrt{f_m t_c}}. \tag{2.36}$$

The relative uncertainty of the effective gain, G', derived from one of the calibration measurements is the same as that of the system temperature measured for time t_c, so the uncertainty in a calibrated measurement of an unknown temperature (that is, after dividing the measured diode output voltage by G' and subtracting the receiver temperature) will be

$$\sigma_T = \sqrt{\frac{(T + T_{rec})^2}{f_m} \left(\frac{1}{t_c} + \frac{1}{t} \right) + \frac{(2T_{rec})^2}{f_m t_c}} \tag{2.37}$$

It appears that the calibration contributes a non-negligible uncertainty to the temperature measurement but that this contribution can be made small by measuring the calibration source for a long time $t_c \gg t$.

2.6 $1/f$ Noise and Gain Variations

As it turns out, calibrating a real radiometer is not as simple as taking long measurements of stable known sources. The problem comes from the fact that the radiometer response itself (the total effective gain) is not stable for long periods of time. Temperature related changes in the gain of the detector diode, RF amplifier and baseband electronics can be mitigated by stabilizing the physical temperature of the

receiver.[20] But there is another source of low frequency noise called $1/f$ noise present in MODFET devices. It is thought to be due to barrier hight and carrier number fluctuations (effecting the gate current and drain current respectively[21]) caused by trapping and detrapping of electrons in trap states. The gate current fluctuations arise from three known mechanisms with a $1/f$ dependence: thermal activation, tunneling, and 2D random walk of electrons into or out of trap states. The drain current is related to the fluctuation of the occupancy (per unit area) of trap states S_{N_t} [15],

$$S_{N_t} = (1/f)kTN_{t_{eff}}, \tag{2.38}$$

by the transconductance, the barrier capacitance and the cross sectional area. Here $N_{t_{eff}}$ is the effective trap density.

$1/f$ noise in the front end amplifier causes gain fluctuations. The relative uncertainty of the radiometer output voltage (or equivalently the relative temperature uncertainty) can be written in terms of the relative gain[22] fluctuations $\frac{\delta G}{G}$, and the relative measurement uncertainty $\frac{\sigma_T}{T_{sys}}$ from the radiometer equation.

$$\frac{\delta V}{V_{dc}} = \frac{\delta T}{T_{sys}} = \sqrt{\frac{1}{f_m t} + \left(\frac{\delta G}{G}\right)^2} \tag{2.39}$$

In the narrow bandwidth limit (also in the limit of short integration time) this reduces to the radiometer equation. Since the gain fluctuations have a 1/f dependence, this is the case at frequencies well above the knee frequency, allowing for an accurate measurement of the thermal white noise level in the power spectrum. For relatively

[20]Variations in atmospheric temperature is another source of uncertainty, but since it is not due to the radiometer it isn't discussed here

[21]The gate and drain current $1/f$ noise are independent.

[22]This is the effective gain G', just dropping the prime.

large measurement bandwidths the noise is dominated by gain fluctuations and the above expression simplifies to

$$\delta V = \left(\frac{\delta G}{G}\right) V, \tag{2.40}$$

at least on timescales $\Delta t > \frac{1}{f_{knee}}$, where the knee frequency f_{knee} is defined as the frequency at which the spectral noise power from gain fluctuations is equal to twice the white noise level. Below the knee frequency the power increases, with larger amplitude gain fluctuations on longer time scales.[23]

The knee frequency of the front end amplifier is below 10Hz. This means that after 0.1 seconds the uncertainty in the temperature due to gain variations is twice the uncertainty from thermal noise σ_T. This is a serious problem for observations of any meaningful duration.

The standard way to mitigate the problem of gain variation is to chop [5], or switch the input to the front end amplifier between the signal and either another source or a calibration target. If the chop rate is fast enough, the gain will not change appreciably during one switch cycle and the signal can be compared to the second input. Simply taking the difference between the two inputs can greatly reduce the 1/f noise. This method resembles the operation of a lock-in amplifier, which reduces noise by multiplying a modulated signal of known carrier frequency by a local oscillator of the same frequency and integrating. In this case, the carrier frequency is the chop rate and the signal is measured relative to the second input.

$$(V_1 - V_2) = (T_1 - T_2)(G + \delta G) \tag{2.41}$$

[23]On very long time scales gain fluctuation are dominated by the physical temperature related gain changes in the backend.

where T_1 and T_2 are the real temperatures of the two inputs to the receiver. In the case of a polarimeter [22] they are the temperature of two orthogonal polarization states, and in the case of a radiometer they are the sky signal temperature and either a reference load or another sky signal from a different part of the sky, usually taken just a few beam widths away from the first sky source.

The desired term is $(T_1 - T_2)G$, which is the differential signal multiplied by the system gain. The second term $(T_1 - T_2)\delta G$ is the residual fluctuation. This term is never zero but if the temperature difference small enough it becomes negligible. For this reason a reference load with a temperature that is very close to the signal temperature (a balanced load) is desired. When the modulation is between two sky signals this condition is easily met.

When taking the difference of two temperature measurements, the thermal noise increases as,

$$\sigma_{\Delta T_{off}} = \sqrt{\sigma_{T_1}^2 + \sigma_{T_2}^2}, \tag{2.42}$$

where ΔT_{off} is the temperature offset $T_1 - T_2$. If the second input is a reference load and not a sky signal, the total time integrating the signal is cut in half, also increasing the noise. Including this noise increase and the effect of a non-zero temperature offset, the uncertainty of the demodulated of a Dicke radiometer is

$$\frac{\delta V}{V} = \kappa \sqrt{\frac{1}{f_m t} + \left(\frac{\Delta T_{off}}{T}\right)\left(\frac{\delta G}{G}\right)^2}, \tag{2.43}$$

where κ is the Dicke switch efficiency, with $\kappa \geq 2$ (depending on the load temperature) when using a reference load and $\kappa \sim \sqrt{2}$ when using two sky inputs.

In a balanced system the 1/f noise is minimized, but this condition is difficult to achieve with a reference load ($T_2 = T_L$) as the sky temperature is always changing. But

taking the difference is only one way to reduce the uncertainty from gain variations. Since modern DAQs can record data at rates much higher than the chop rate, the demodulation is done on a computer, so it should be just as easy to measure the instantaneous gain $(G + \delta G)$ itself during each chop period, and use it find the signal temperature directly. If the reference load temperature is known and stable it is straightforward to find the gain from

$$V_L = T_L(G + \delta G). \tag{2.44}$$

Then, the value of T_{sky} can be determined by dividing by the gain. The resulting uncertainty of the demodulated sky temperature is given by

$$\frac{\sigma_{T_{dem}}}{T_{dem}} = \sqrt{\left(\frac{\sigma_{V_{sky}}}{V_{sky}}\right)^2 + \left(\frac{\sigma_G}{G}\right)^2}, \tag{2.45}$$

where V_{sky} is the diode voltage when looking at the sky signal and T_{dem} is the demodulated output of the Dicke radiometer (note that this is the full temperature, not the offset temperature). The relative uncertainty of the voltage measurement is again just the relative uncertainty from thermal noise of the sky temperature, and the relative uncertainty in the gain measurement $\frac{\sigma_G}{G}$ (note that this is not the relative gain fluctuation term $\frac{\delta G}{G}$) is the same as the relative uncertainty in the thermal noise $\frac{\sigma_{T_L}}{T_L}$, so the relative uncertainty is

$$\frac{\sigma_{T_{dem}}}{T_{dem}} = \sqrt{\left(\frac{\sigma_{T_{sky}}}{T_{sky}}\right)^2 + \left(\frac{\sigma_{T_L}}{T_L}\right)^2}. \tag{2.46}$$

The uncertainty in the demodulated output T_{dem} after dividing by the gain is the same as the uncertainty when taking the difference in a balanced system (twice the thermal noise when using a reference load). This is true even if the offset between

the sky and load temperatures is large. But the uncertainty is not so simple.

Measuring a small noise component on a relatively large signal is limited by the DAQ dynamic range. In a differential system only the offset temperature is measured, but measuring the gain requires knowing the full diode voltage. To overcome this problem a known voltage offset can be introduced in the baseband electronics in order to bring the voltage into the DAQ range. This offset has an unknown but fixed error. Adding a fixed offset error ΔV to the output voltage

$$V_{out_L} = T_L(G + \delta G) + \Delta V \tag{2.47}$$

gives an output sky temperature that depends on δG, ΔV and the two temperatures

$$T_{out_{sky}} = T_L \frac{T_{sky}(G + \delta G) + \Delta V}{T_L(G + \delta G) + \Delta V}. \tag{2.48}$$

The relative error on this temperature is complicated[24], but it is clear that in the limit as δG, ΔV, or $(T_{sky} - T_L)$ go to zero, the uncertainty goes to zero. Even if the voltage offset error is extremely small, a large temperature difference between source and reference presents the same problem with dynamic range that was the reason for introducing the offset. But if the temperature difference is not prohibitively large and the voltage offset is well understood it would be possible to use a gain measuring based approach to get very good $1/f$ performance without a balanced load.

A different approach to removing $1/f$ is a noise adding system in which some known amount of noise is periodically added to the antenna temperature. The two modulated components are T_1 and $(T_1 + T_2)$, where T_2 is the added noise. The gain

[24]Taking the difference of two measurements of the same sky temperature at two different gains (as would be the case for gain drift) gives $\frac{\delta T_{out_{sky}}}{T_L} = \frac{\Delta V}{V_L}\frac{\delta G}{G}\frac{\Delta T}{T_L}$, where ΔT is just $(T_{sky} - T_L)$

is found by first subtracting to find V_2, then dividing as before.

The noise is inherently worse than in the previous systems

$$\frac{\sigma_{T_{dem}}}{T_{dem}} = \sqrt{\left(\frac{\sigma_{T_{sky}}}{T_{sky}}\right)^2 + \left(\frac{\sigma_{T_{add}+T_{sky}}}{T_L}\right)^2}. \tag{2.49}$$

Noise adding could also be used to artificially balance a load in a traditional Dicke radiometer. Low loss couplers have been shown to work for adding a small amount of noise to the antenna temperature without seriously increasing the receiver temperature.

Chapter 3

RFI

There are numerous hot, narrow band radio-frequency interference (RFI) sources throughout the receiver gain band. The sources, presumed to be located on towers in the mountains to the North of Santa Barbara and on satellites in Geo-stationary orbit around earth (and possibly in the Airport less than a mile from the UCSB campus) are a few orders of magnitude hotter than astronomical sources and can add a significant amount of power to the telescope beam, even if they only illuminate the side-lobes. It is therefor crucial to identify and remove all significant sources of RFI in order to make a sensitive measurement of the sky.

RFI sources will generally be fixed in the earth frame while astronomical sources will not, instead exhibiting diurnal motion. This makes it easy to detect the presence of RFI in the data and could make it possible to distinguish it from astronomical sources and to remove it. Sources that are not stationary, such as transmitters on airplanes or police cars and sources that transmit intermittently could be more difficult to identify, but would permit at least part-time interference-free observation.

3.1 Textronix Spectra

The observed RFI sources transmit in narrow bands and are easy to spot with a spectrum analyzer. A Tektronix 2754 programmable spectrum analyzer was used together with a GPIB card to record a large number frequency sweeps in different bands to look for RFI. The spectrum analyzer was connected to the output of the receiver with the front-end cooled and the back-end in the original configuration (two back-end amplifiers followed by a 2.4GHz wide band-pass filter).[1] The band pass filter, which is visible in figure 3.1, was chosen to have a band width equal to 30% of the center frequency, roughly the same as the feed horn, but it is clear that much of the band may be unusable due to radio interference.

There are 167 sweeps plotted in figure 3.1 with power measured in 5MHz bins from 5.5 to 10.5GHz. The horizontal axis is frequency and the vertical axis is power[2] (P) in dBm.

$$P(\text{dBm}) = 10\left(\log\frac{P[\text{mW}]}{1[\text{mW}]}\right) \tag{3.1}$$

There are a large number of spikes around 7GHz, some of which are 25dB above the thermal noise level. Above 8GHz there are only a few visible spikes, but there is also an undesirable dip in the power at 9GHz[3]. Below 6.5GHz and above 9.5GHz the power from the receiver is attenuated enough that, except for a few spikes, it is below the spectrometer noise floor, which appears around -65dBm. The 2754 specifications give an equivalent input noise of -70dBm (275412754P Service Vol.1, p. 2-11) between 5.4 and 12.0GHz with 1MHz resolution band-width, or bin size.

[1] This configuration makes the last stage amplifier most susceptible to compression since the input power band is not restricted before amplification.

[2] This is the power out of the receiver as measured by the the spectrum analyzer

[3] This dip could be due to the horn response.

Figure 3.1: Plot of 167 sweeps 5.5 to 10.5GHz

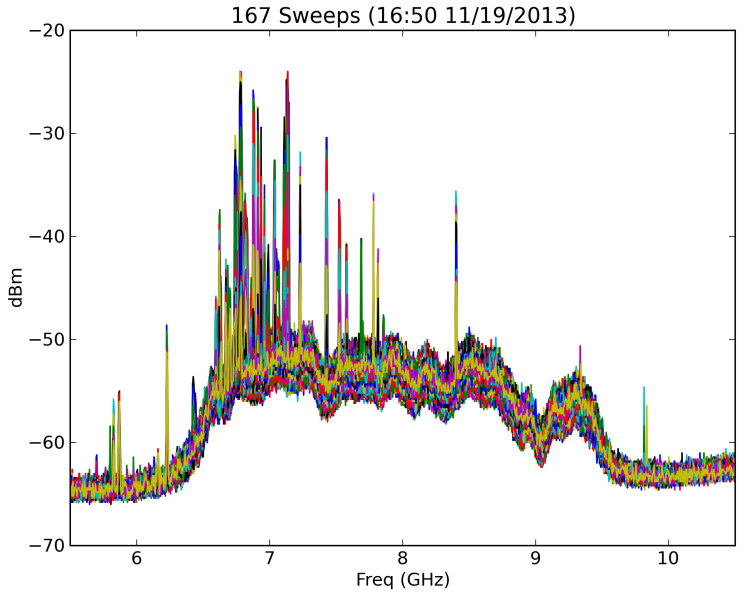

The sweeps in this plot were taken with 5MHz bins, and though the specifications don't provide a sensitivity for 5MHz bins, the spectrometers equivalent input noise increases linearly with bin size, so a noise floor just above -67dBm is expected[4].

3.2 Broadcast Peak

This data was collected with the telescope rotating slowly in azimuth from North to West with an elevation of about 10 degrees above the horizon so that for part of the scan the beam points directly towards Santa Barbara's broadcast peak. The plot is very good at highlighting spikes in the power, but because all of the sweeps are drawn on top of each other it is difficult to distinguish between them even though the beam direction is changing.

Figure 3.2 shows an image of the same data drawn again with frequency along

[4]The EIN for instruments with Option 01 is -65dBm for a 1MHz RBW

the horizontal axis, but with sweep number along the vertical axis and power given by a gray scale (still in dBm). The spikes that appear in the plot (Figure 3.1) are visible here as vertical lines of various length.[5] It is clear that these spikes do not appear in all of the sweeps. Most of the RFI power is near the middle of the azimuth scan, when the beam was pointing toward broadcast peak. The first 20 sweeps at the bottom of the image were recorded while the beam was pointing at a wall to the North. The thermal noise level is higher as expected, but there are also spikes here that are not visible in the rest of the scan. These are most likely from sources behind the telescope being reflected off of the wall.

In order to better understand this data it is useful to gather some information on the sources themselves. The FCC has allocated the bands between 6GHz and 8GHz for fixed and mobile satellite communications. One of the FCC rules specifically for wide-band systems gives a peak EIRP[6] of $20\log(\mathrm{RBW}/50)$dBm, where RBW is the resolution band-width in MHz (FCC Rules, section 15.250). For RBW = 5 this equation gives a peak EIRP of -20dBm The sources on broadcast peak are 17km away from the telescope located on the roof of Broida hall on the UCSB campus. Taking the collecting area to be 1 square meter, the ratio of the EIRP to the collected power is $10log_{10}(1/(4\pi(17\times10^3)^2)) = -95dB$, which suggests a total receiver input power of -115dBm.

The thermal noise power in a 5MHz band from a low elevation sky (assume a 50K system temperature) is also -115dBm. The RFI power is $\sim$ 20dB above the thermal level, so clearly these transmitters are not operating under the rule stated above.

[5]The spectrum analyzer measures 1000 frequency bins in each sweep, so the image is 1000 pixels wide. The vertical axis is stretched to make the image appear square, so for a set with fewer than 1000 sweeps the vertical pixels all appear taller than the horizontal pixels are wide by a factor 1000/#sweeps.

[6]EIRP is the total output power of an isotropic emitter with power per unit solid angle equal to that of the actual antenna in the direction where its gain is maximum. It is equal to the actual total output power in dBm plus the gain (relative to an isotropic emitter) in dB

Figure 3.2: Image of 167 sweeps 5.5 to 10.5 GHz

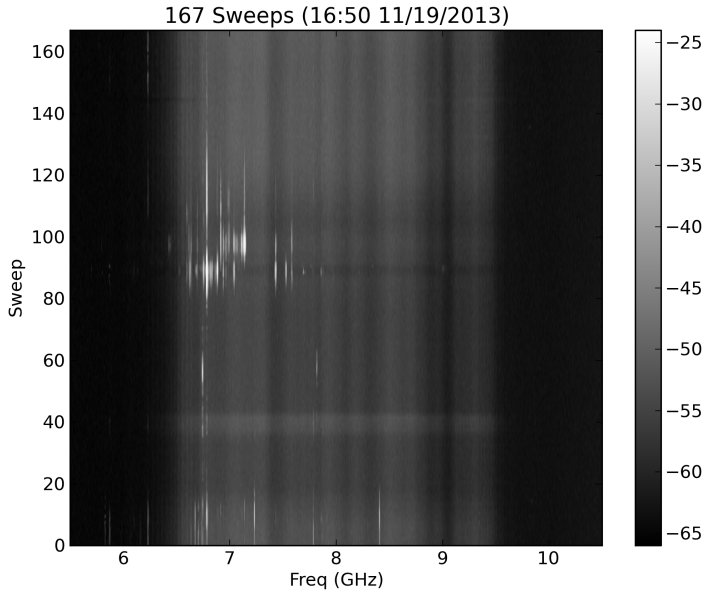

The figure indicates that the thermal level is at about -53dBm, corresponding to a total receiver gain (including the lossy cable that brings the signal to the spectrum analyzer) of 62dB, which is reasonable. This suggests a peak receiver input power from RFI on the order of -90dBm (in a 5MHz band), corresponding to an EIRP of 5dBm.

Figure 3.3 is another scan across broadcast peak, this time looking at a 1GHz wide part of the spectrum centered on 7.0GHz. The frequency bins are now 1MHz wide (instead of 5MHz). The frequencies with RFI seem to match those in Figure 3.1, but in this scan there is a lot more variation in the thermal noise level from one sweep to the next,[7] which could easily obscure smaller RFI spikes. Also, the vertical scale on the spectrum analyzer is 5dBm/div, not 10, so the big spikes are cut off.

[7]The expected thermal level would be $\sim$ 7dB below the level in Figure 3.1 due to the smaller RBW.

Figure 3.3: Plot of 125 sweeps 6.5 to 7.5 GHz

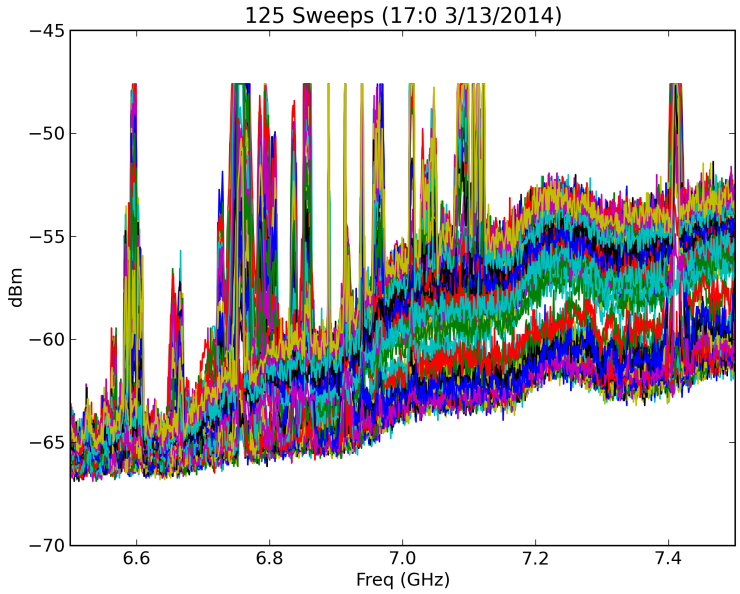

3.3 The Diff

One way to isolate the spikes is to diff the data. Diff is a Numpy[8] operation that takes the difference of each point in an array and the next point in that array (in the case of a first order diff) to create a new array that is a discrete derivative of the data[9]. Figure 3.4 is the plot of the absolute value of the diff (in dB) of the data in Figure 3.3 versus frequency. It is very easy to identify spikes in the plot of the diff.

Using the diff data it is possible to find every spike of a given size (above the thermal noise) in every sweep. Since every sweep of the spectrum analyzer may be measuring RF power from a different point in space, the thermal level and therefor the noise may be different from sweep to sweep so the spike threshold is set relative to the standard deviation for each sweep.[10]

[8]Numpy is a standard math package for Python.

[9]For the data analyzed here it is useful to take the second order diff (the difference of each point from the point two up the list) since not all spikes reach their full amplitude in one step.

[10]The standard deviation should be calculated only for the thermal noise, without the spikes, so

Figure 3.4: Diff of 125 sweeps 6.5 to 7.5 GHz

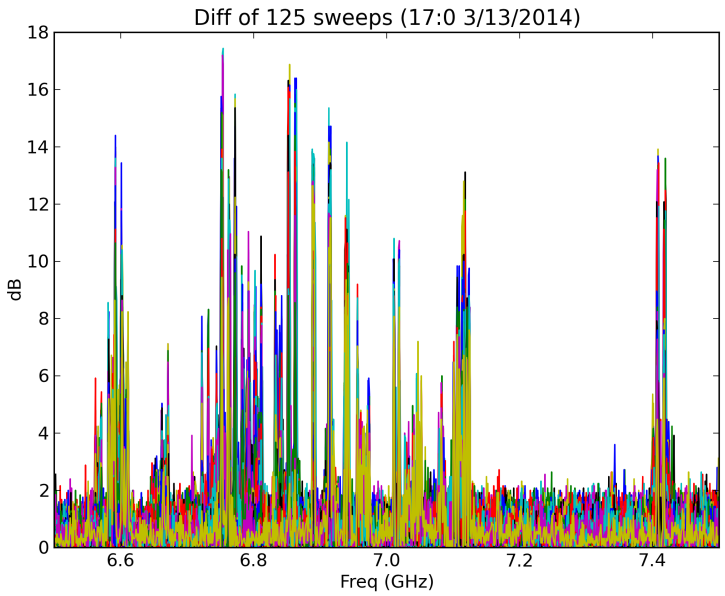

The plot in figure 3.5 has in the vertical axis the total number of spikes detected (above 3 times the standard deviation) in each frequency bin, divided by the number of sweeps in the scan, giving the fraction of sweeps with spikes. This plot looks very similar to the diff plot for this scan. The noise in this plot comes from the fact that the threshold was set low to make sure that even small spikes were detected. If the threshold was set higher the plot would only include real spikes, but the number of false positives here is small and on average should be uniform across the band. A list of frequencies at which RFI is detected for a non-negligible fraction of the time can easily be produced from this data, but the list for this scan is very long and is not printed here.

large spikes (in this case above 3dBm) are not included.

Figure 3.5: Diff of 125 sweeps 6.5 to 7.5 GHz

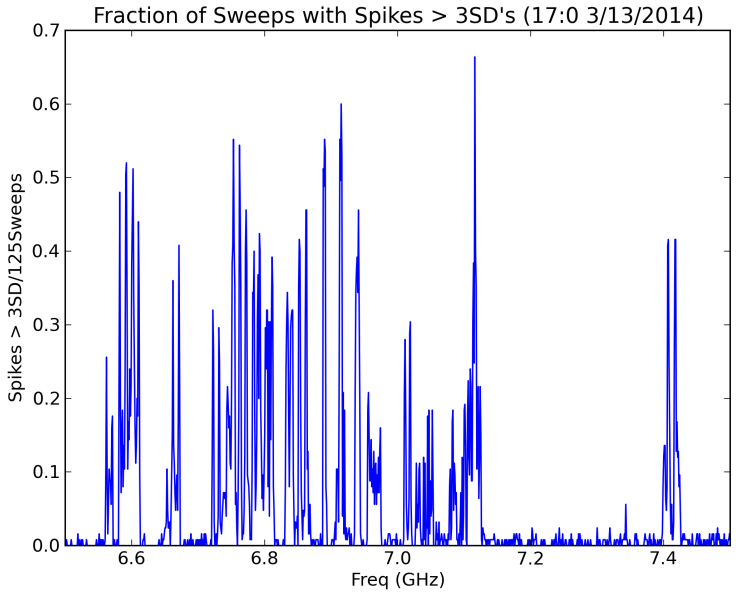

3.4 Satellites

The other known fixed sources of RFI are transmitters on geostationary satellites. Only two satellites were found to transmit in the receiver band. They are located West of South by about 10° and about 40° about the horizon. They were found not by using the spectrum analyzer but by looking at the total integrated power using a detector diode. The search covered a range of 120° in azimuth and 20° in elevation, leaving some unexplored regions near the horizon.[11]

Figures 3.6 and 3.7 show plots of a small number of sweeps taken with the telescope pointed directly at the two satellites respectively. Their spectra around 7GHz are similar to each other, and different from those of broadcast peak. Figure 3.8 shows a plot of satellite 2 data around 8GHz. The majority of the power from these satellites is found between 7.25GHz and 7.75GHz, which corresponds to the wide-band global

[11]Since the search was done only looking at the diode output while scanning the beam around in the sky it is possible that weak sources were overlooked.

Figure 3.6: 23 sweeps on satellite 1, 6.5 to 7.5 GHz

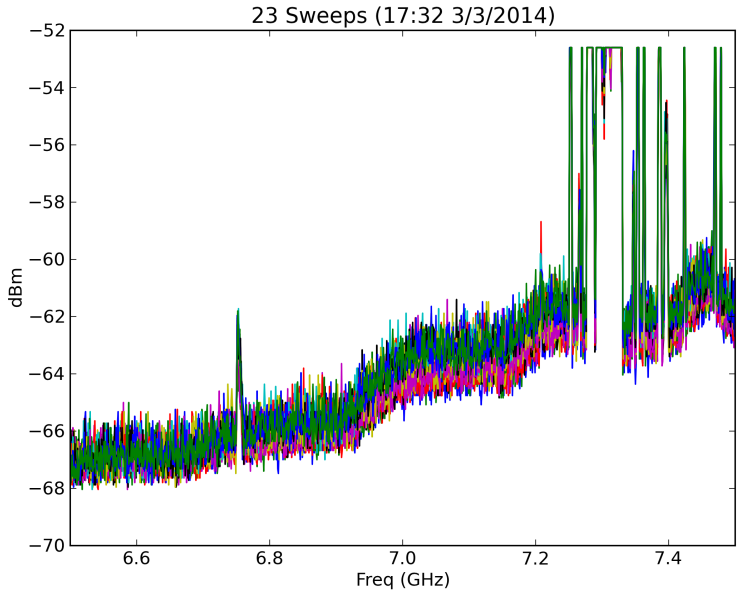

SATCOM (WGS[12]) systems X-band down-link (from http://spectrumwiki.com, FCC 5.461). The satellite spectra appear to be free of RFI above 7.8GHz except for 1 spike at 8.4GHz. In the spectra taken on broadcast peak this feature has a much larger amplitude suggesting that the spike at 8.4GHz may not be coming from the satellite but from side lobe pickup.

3.5 Side Lobe Pickup

During normal observing mode (for acquisition of astronomical data) the beams main lobe points at an elevation angle of around 45 degrees (above the horizon, and broadcast peak). This angle is close to the elevation angle of the geostationary satellites, but there is enough freedom in the choice of observing elevation that they can be avoided by at least a few degrees. Even if the beam is not pointed directly at

[12]WGS is a military satellite communications network that operates in X-band and Ka-band.

Figure 3.7: 27 sweeps on satellite 2, 6.5 to 7.5 GHz

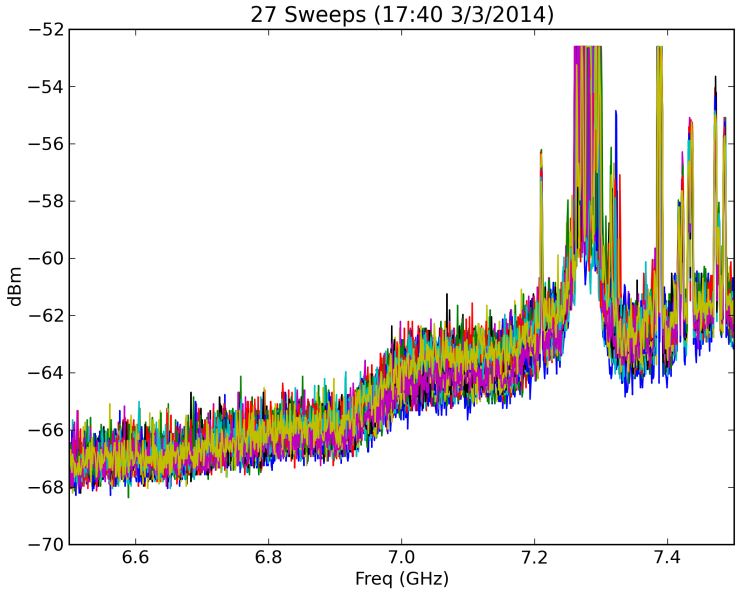

Figure 3.8: 29 sweeps on satellite 2, 7.5 to 8.5 GHz

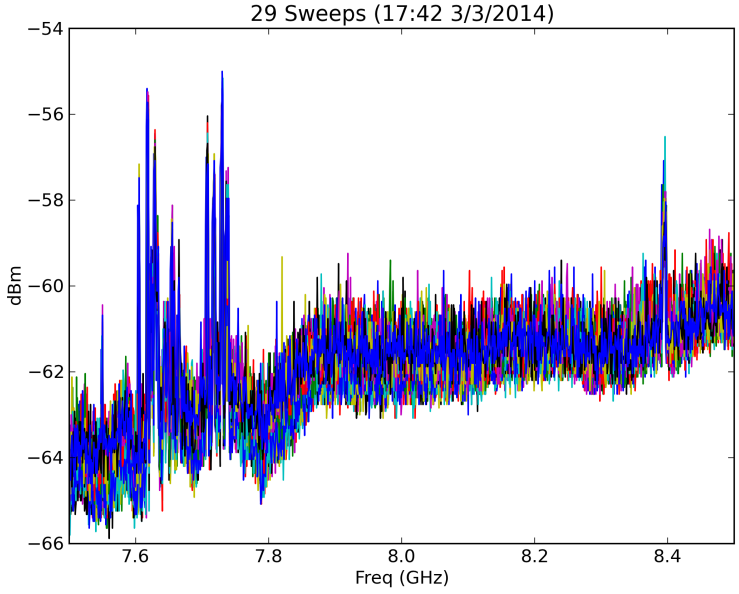

Figure 3.9: Plot of 2333 sweeps 6.5 to 7.5 GHz

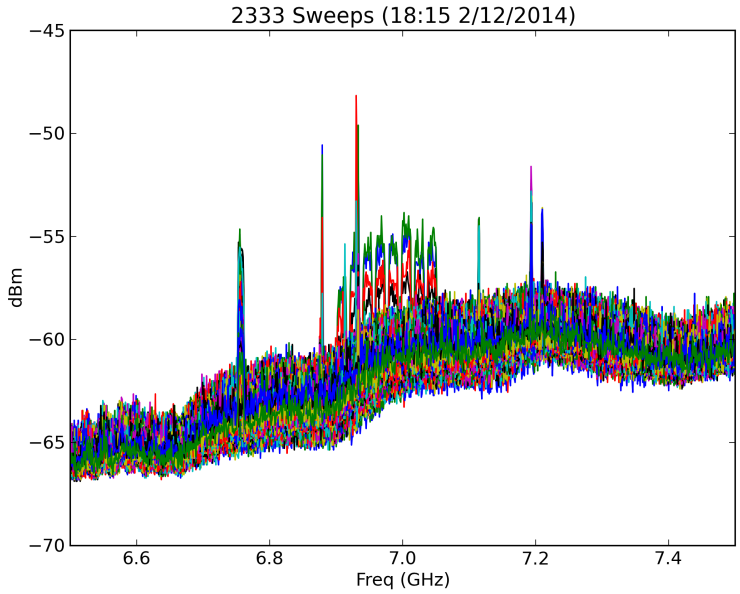

sources of RFI, some of the the power from these sources can find its way into the telescopes side lobes. In order to find how much of this power is picked up by the receiver in an observing configuration several long spectral data sets were taken with the beam pointing approximately 45 degrees above the horizon.

Figure 3.9 shows a plot of an azimuth scan at nominal elevation with a rotation rate of about 1 revolution every 8.5 minutes. There are several spikes appearing below 7GHz that may well come from broadcast peak, but there is one just below 7.2GHz that does not appear in any of the previous data, which suggests that there are unknown sources in addition to those already investigated.

The gray-scale image of this data in figure 3.10 has a few interesting features. This set has many more sweeps than the sets taken looking at RFI sources, so the vertical scale in the image is not stretched but rather compressed compared to the horizontal. Many of the spikes are present throughout all seven rotations of the telescope, but one spike, just above 6.9GHz seems to turn on during the fifth rotation. There is

Figure 3.10: Image of 2333 sweeps 6.5 to 7.5 GHz

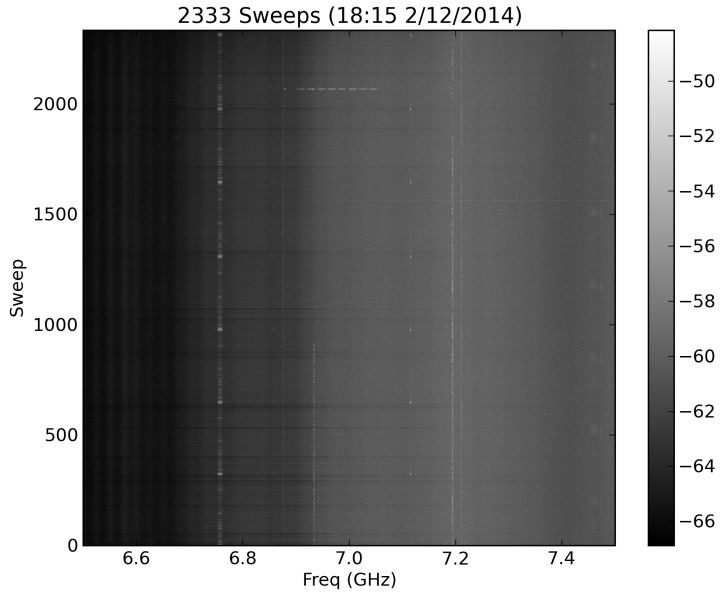

also a set of bands that appears only briefly during the first rotation. These sources appear to be transient. As mentioned before, the impact of transient sources on the astronomical data depends on the duty-cycle, and data collected while these sources are transmitting can be thrown away.

One troubling feature is a faint wide-band source near 7.5GHz that appears in every rotation. This feature is undetectable in the plot, barely visible in the diff (not shown here), and completely missing from the list of detected spikes. Two possible explanations for this absence are that the change in power vs. frequency is too slow to give an appreciable value in the diff (even in the second order diff), and or that the threshold for detecting spikes is set too high to detect the small change in power. Applying a third order diff to all of the data would have the effect of widening spikes by 2MHz[13] and lowering the threshold would increase the number of false positives.

[13]A spike in a third order diff will appear to rise one bin before and fall one bin after the same spike in a second order diff. The second order diff also broadens spikes by two bins compared to the first order diff.

Figure 3.11: Plot of 3451 sweeps 7.5 to 8.5 GHz

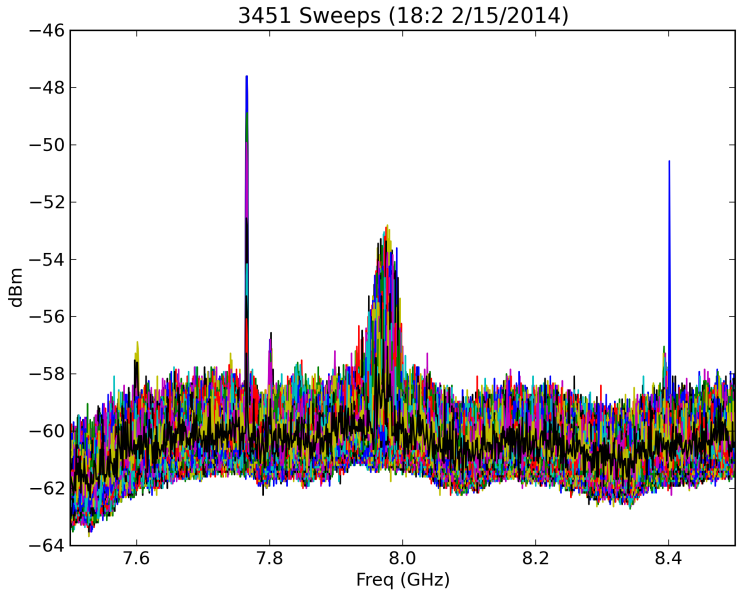

The human eye is capable of detecting this feature in the image, so the easiest solution here is just to look.[14] Lowering the detection threshold to 2 standard deviations does make this feature visible (though just barely) in the plot of the spikes, and taking a third order diff brings the detection fraction to 5% above the noise count level.

The data plotted in figure 3.11 includes 3451 sweeps also taken at about 45 degrees elevation. This plot reveals a relatively wide transmission band centered just below 8GHz that was not detected while looking at either the satellites or broadcast peak. It appears to be present with relatively constant brightness in every sweep in the image (not shown here), so the source direction is unknown. The presence of RFI not accounted for in the spectra of either of the known sources is alarming. It means that, though this source is bright enough to be easily detected, there may be other less bright sources that are overlooked.

[14]The feature also corresponds to spikes in the satellite data, so it is actually already accounted for.

3.6 Sensitivity

The contribution of a potentially unidentified RFI source to the astronomical data is easy to determine. In a normal data-taking mode the radiometer output is proportional to the total integrated power in the filter pass band. The increase in the output caused by a narrow band RFI source is simply its spectral power times its band-width divided by the filter band-width. For example, a source with the same spectral power as the thermal (system) power level would double the power in its own band producing an easily detectable 3dB bump or spike in the spectrum. If this source has a 1MHz band and the radiometer has a filter with a 1GHz band width, it would increase the radiometer output by 0.1 percent.

Assuming the spectrum analyzer measures at 100% duty cycle, each 1MHz bin is measured for about 5ms. The radiometer equation predicts a relative error of about 1.4 percent, but the standard deviation of the noise in each sweep (with spikes removed) is about 0.6dB, or about 14 percent. This means that a 1MHz source with spectral power one tenth the thermal power (which would produce a 0.4dB bump) would be undetected in the spectrum.

The relative uncertainty of a receiver with a 1GHz bandwidth and a 1kHz low pass filter (for 1ms of integration) would be 0.1 percent so a 3dB spike, though not visible in the raw radiometer output, would show up after about 25ms of integration. This means that the spectrum analyzer taking sweeps with a 1MHz resolution band-width is just barely capable of detecting the presence of RFI that would affect the radiometer output after short integration times. A 1 second integration time would allow the radiometer to detect sources of RFI (that transmit for the entire integration period) 16% above thermal, which is right at the spectrum analyzer noise level.

Figure 3.12: Plot of mean Diff of 3451 sweeps 7.5 to 8.5 GHz

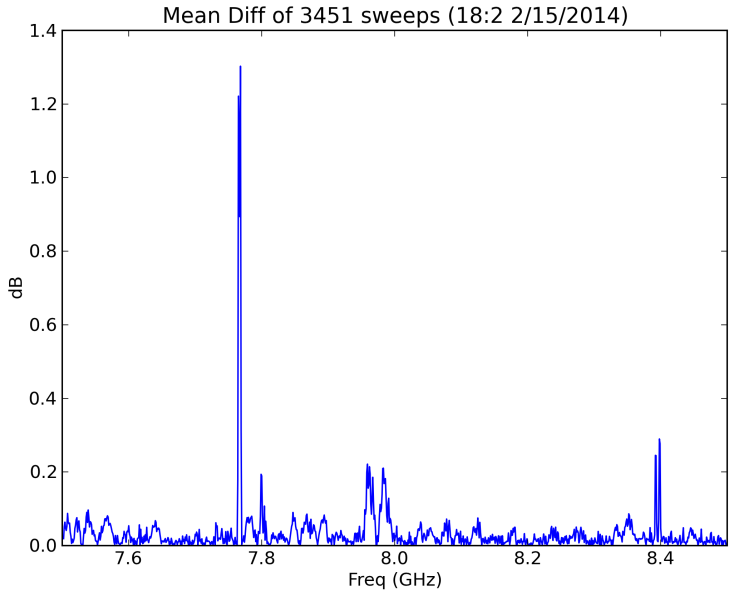

The only way to improve this data is to integrate.[15] Since the data set plotted in figure 3.11 has so many sweeps, an average over the sweeps could provide a significant improvement in sensitivity for certain spikes. Taking the mean (along the sweep axis) of the diff[16] of the data highlights spikes that are present in a large fraction of the scans while suppressing transient or directional RFI (the telescope rotation rate and sweep rate were independent). Figure 3.12 shows a plot of the mean of the diff. The noise is reduced and several questionable bumps are now visible. These could be due to bumps in the frequency response of the receiver or the spectrum analyzer, but they could also be low-power wide-band RFI.

In order to improve the sensitivity to directional spikes a large number of sweeps

[15]Since noise floor of the spectrum analyzer is roughly proportional to resolution band-width, taking data with 100kHz bands may improve the sensitivity, but only for sources narrower than 1MHz.

[16]One important benefit of using the diff data is that only time intervals of the period between samples (a few ms) is important. This means that the amplifier 1/f noise present in the diff data is the same as a receiver with a Dicke switch operating at few hundred hertz.

would need to be taken in every direction. Even with this increase in sensitivity, there is no certain real way to ensure that the data will be free of RFI.

3.7 RFI Filters

In spite of the presence of a large amount of RFI in the receiver band, it may be possible to limit the output band to a range with no spikes, or to filter out the spikes with notch filters. After reviewing all of the data the best range seems to be from just above 8GHz to just above 9GHz. Figure 3.13 shows the upper half of this range. As band pass filters with specific cutoff frequencies are expensive and take a long time to make, it turned out that the fastest and cheapest way to choose a band was to look at existing filters from a surplus shop[17]. The widest band pass filter available in a clear part of the spectrum was 500MHz wide from 8.75GHz to 9.25GHz. This is a 7-pole was made by Reactel. For a naive estimate, assume that each filter pole reduces the transmitted power by 6dB per octave away from the cutoff frequencies, so the power at 18.5GHz should be down by 42dB after the filter, or if the roll-off is flat the power would be down by about 20dB at 14GHz. In reality these filters are much better (Figure 3.14) and power is down by 20 dB at 9.5GHz. This isn't quite enough attenuation, since there are nearly 15dB spikes at 9.3GHz, so two filter stages are used (Figure 3.15).

These band-pass filters turn out to be very effective at removing almost all of the RFI from the receiver output. There remains a transient contribution presumably from the spikes at 9.25GHz, but for the most part the data is free of contamination.

[17]Western Test Systems

Figure 3.13: Plot of 2814 sweeps 8.5 to 9.5 GHz

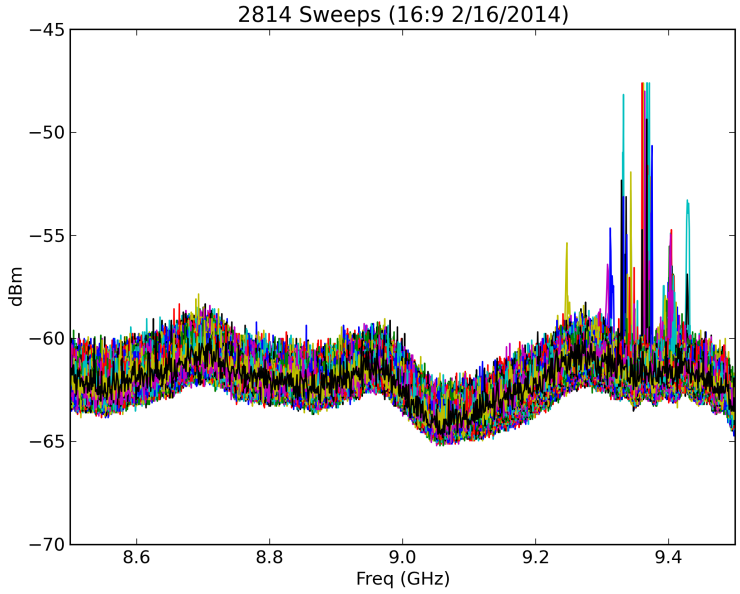

Figure 3.14: Plot of 1 filter S-parameters sweeps 8 to 10 GHz

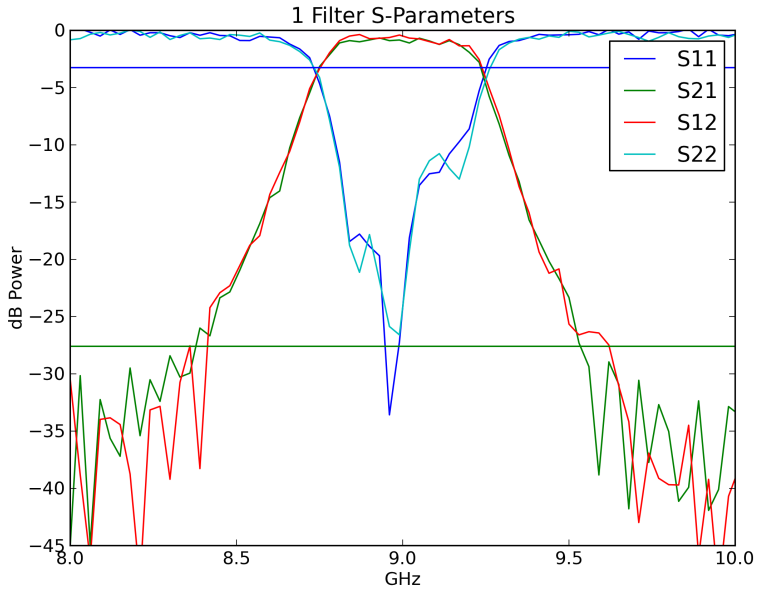

Figure 3.15: Plot of 2 filters S-parameters sweeps 8 to 10 GHz

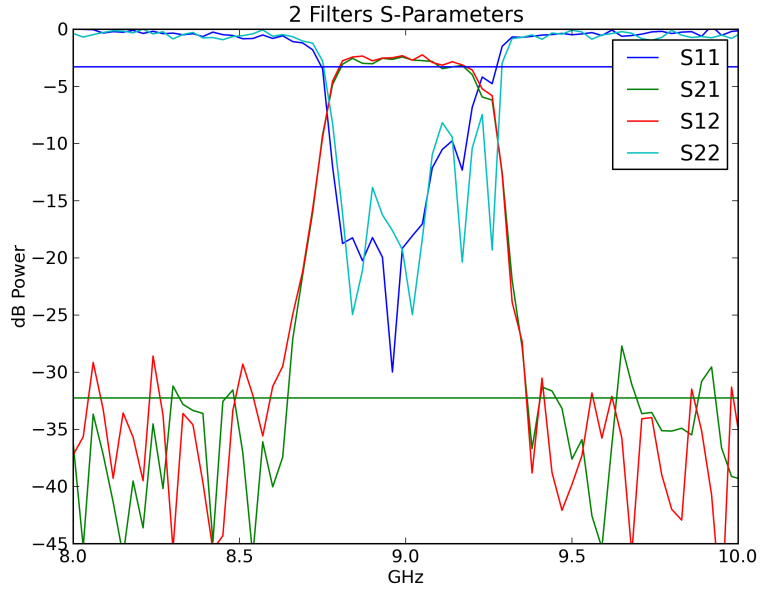

Chapter 4

The Instrument

4.1 Instrument Requirements

The requirements for this instrument are based on the desire to measure the temperature of the diffuse foreground radio emission from the Milky Way galaxy well enough to make a contribution to the understanding of the spinning dust and the haze components that appear in the WMAP data. First, it has to be cheap enough to build and maintain, which rules out a satellite or balloon campaign (a ground based instrument is not limited in size or weight as are instruments deployed into the upper atmosphere, but is limited by atmospheric observing conditions), and it must be reliable enough to make deep maps with sensitivity comparable to the WMAP data. The instrument should also be capable of mapping the galaxy at a resolution sufficient to differentiate the sources of interest from the background.

The instrument should be able to make measurements with a temperature uncertainty of $\sim 30\mu$K to make it comparable to WMAP[17]. A total power radiometer could achieve this level of sensitivity by employing a wide band receiver with a noise temperature of $\sim$ 10K and an integration time of $\sim$ 100 seconds per pixel, which

translates to an observation campaign of a few months.

The preferred observing strategy puts a limit on the allowable gain instability. This strategy is simply to scan a large circle on the sky around zenith in a time period (about a minute) short enough that the part of the sky measured in each scan overlaps with the previous one. This strategy allows comparison of adjacent scans and helps with the removal of gain drifts on timescales longer than the rotation period. Gain instability on timescales smaller than this could be mitigated with a faster rotation rate, but at the cost of more mechanical demands (and a potentially dangerous instrument). A $1/f$ knee at $\sim$ 10mHz would allow for a reasonable scanning rotation rate. Reducing the $1/f$ while maintaining the sensitivity requires a low loss Dicke switch with a balanced (or close to balanced) reference load. This turns out to be the primary challenge in building a instrument with these requirements.

4.2 The Instrument

The LATTE instrument is a radio telescope, or simply, a radiometer with mirrors. A radiometer is any device that measures radiated electromagnetic power. This radiometer measures the total integrated power in a specific band determined by a band-pass filter, from a region in the sky determined by the mirrors and their orientation (figure 4.1).

The LATTE telescope uses the same mirrors and frame as the Cosmic Foreground Explorer (COFE)[8] telescope (figure 4.2). This optical configuration is a folded version of the BEAST optics[1], designed to measure polarization using a reflective polarization rotator plate[2] at the common focus between the primary and secondary

[1]BEAST used a large flat mirror in front of the primary to modulate the beam position in the sky by a few degrees.

[2]The polarization rotator does this by measuring the difference between the power level in one

Figure 4.1: Telescope on the Roof

mirrors. Incident radiation is focused onto the polarization rotator by the primary mirror, then onto the feed horn by the secondary mirror. The mirrors, the polarization rotator and the feed horn comprise the telescope optics.

The feed horn is also the first element of the radiometer. At the end of the feed horn is a circular to rectangular waveguide transition that selects one polarization and reflects the other. It is followed by a waveguide to coax transition that uses a waveguide probe[3] to couple the radiation in the waveguide onto a coaxial transmission line that feeds the receiver.

The receiver chain is the RF part of the radiometer (figure 4.3). It is divided into a cooled front-end section housed in a Dewar (cryostat) along with the feed horn, and a back-end section housed separately. The front-end consists of a PIN diode

polarization state with that in the polarization state orthogonal to it.

[3]Only one polarization component is measured by the waveguide probe. The orientation of this component is fixed unless the rotator is turning. An ortho-mode transducer would allow measurement of both orthogonal polarization components.

Figure 4.2: COFE Optics

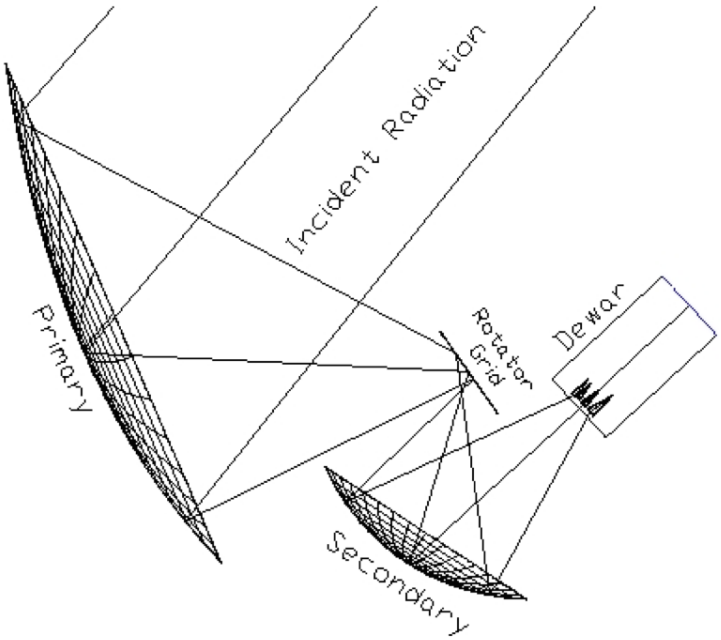

Figure 4.3: Radiometer Block Diagram

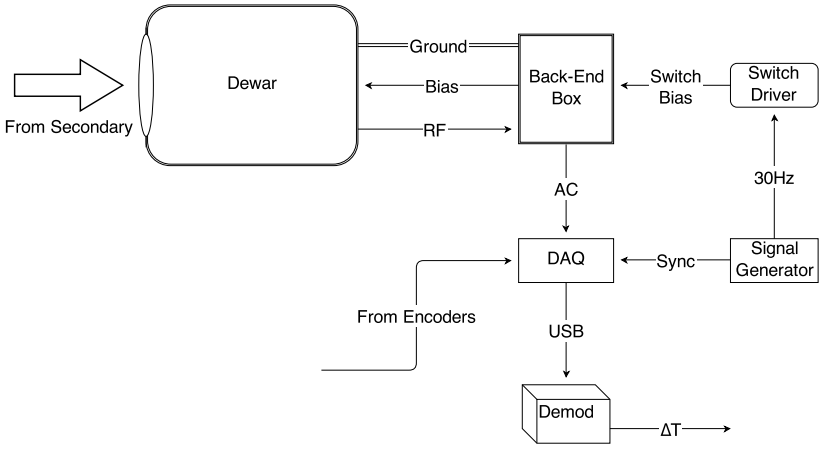

switch (a Dicke switch [5]) that allows the receiver to measure temperature, and the front-end amplifier that provides a large portion of the RF gain and makes the largest contribution to the receiver noise temperature. The two components are cooled to minimize the receiver noise temperature.[4] The back-end includes the band-pass filters that determine the measurement band, the back-end amplifiers that provide additional RF gain, and the square-law detector that outputs a voltage proportional to the incident power. The back-end contributes very little to the receiver noise temperature so all of its components are operated at room temperature.

The receiver output voltage is quite small and requires amplification before it can be recorded by the data acquisition system (DAQ). This is done using operational amplifiers (baseband amplifiers) on circuit boards that are housed along with the amplifier bias circuit boards and the receiver back-end in the back-end box. Figure 4.3 shows the functional connections between the dewar, the back-end box, the DAQ, the signal generator that provides the trigger for the switch, and the switch driver that controls the switch state. After the chopped (or modulated) data is recorded as digital data, it is demodulated on a computer. The demodulated data is the final output of the radiometer.

4.3 Receiver as Planned

Modulating or chopping the signal is what allows the radiometer to mitigate the problem of gain variations (and $1/f$ noise) in the receiver. A Dicke-style switching radiometer chops the signal with a reference load of fixed temperature. The original plan was to have the switch chop between the antenna and an internal cold load (a coax termination) at a physical temperature that would be actively driven to match

[4]The feed horn is also cooled to reduce the noise temperature and is mechanically attached to the front-end.

the sky temperature.

The standard two-stage CTI cooler used to cool the dewar has a lower limit second stage temperature of about 10K, and when loaded runs at closer to 20K. This is cold enough to minimize the front-end amplifier noise, but as the sky temperature is in general less than 20K, a balanced load would have to be cooled by some secondary method. Two methods were considered during the dewar design process. One option was to use a Cryomech pulse tube cooler (in addition to a CTI[5]) with a cooling power of 1W at 4.2K (figure 4.4 shows this option). The cold stage of this cooler would be thermally connected to the cold load well enough to cool it below the sky temperature and then, by some other means, be heat it to match the sky temperature (assumed to be above 4.2K). The other option for cooling the load to the sky temperature would have been to include a liquid helium "bomb" dewar in the larger dewar assembly, which would be attached to the cold load instead of the pule tube cooler. Both of these options were eventually abandoned.

Another element of the receiver that was changed from the original design was the band-pass filter. The original band-pass for the receiver was chosen to be 30% of the center frequency, which at 8GHz would provide a measurement band wide enough to achieve the desired sensitivity, while still narrow enough to distinguish it from neighboring bands for measuring spectra. 2.4GHz wide band pass filters were actually purchased from K&L microwave and installed before the severity of the RFI problem was fully understood. The original design for the back-end is sketched in figure 4.5.

[5]In order to accommodate two coolers on a single dewar, the cooler ports were arranged on the lower part of the circular side wall of the dewar. This arrangement turned out to be quite inconvenient.

Figure 4.4: Front-end as Planned

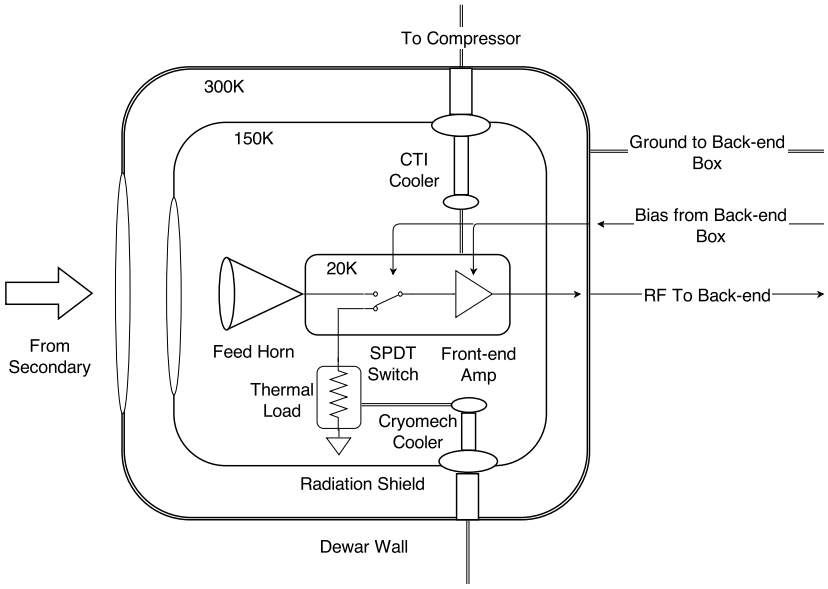

Figure 4.5: Back-end as Planned

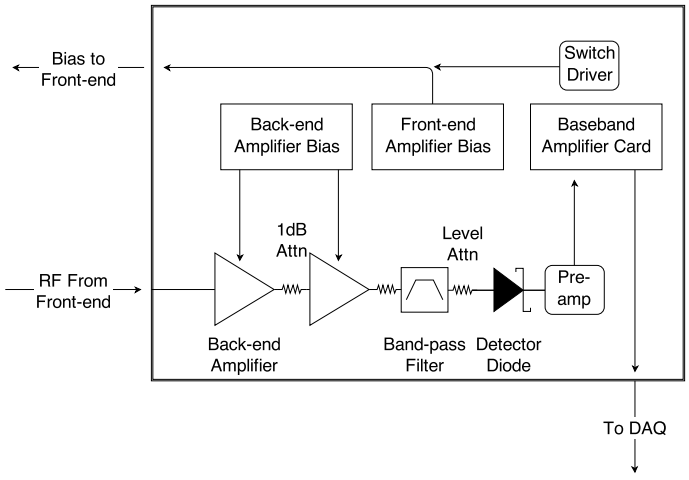

4.4 Instrument as Built

The first major problem in implementing the design described above was finding a low loss switch that would work reliably at cryogenic temperatures. In order to chop between the sky and a thermal load a single-pole double-throw (SPDT) switch would be required. The only SPDT switch shown to work reliably at 20K has a loss of about 2dB ($\sim 40\%$) when cooled, which is far from ideal. Instead a reflective SPST (single throw) switch with less than 1dB of loss is used.

The SPST switch either transmits or reflects radio power. In the transmission mode it brings the sky signal from the feed horn to the front-end amplifier, and in reflection mode, it reflects the front-end amplifier input noise temperature back to itself. The amplifier input noise functions as an active cold load [12]. The downside to this approach is that the amplifier input noise cannot be changed to balance it with the sky temperature, but this turns out not to be a problem.[6] A benefit of using an active cold load is that there is no need for an expensive and complicated pulse tube cooler or a load with a physical temperature equal to that of the sky, which allows for a simpler dewar and receiver design (figure 4.6).

The other major problem with the original design was the pass band. It was assumed that RFI could be removed with the use of a number of notch filters, but it turns out that the 6 to 10GHz band is heavily used by transmitters operating in Santa Barbara as well as on satellites in geostationary orbit (for details see RFI chapter). A combination of high-pass, low-pass and notch filters to remove RFI and maximize the usable integration band was considered, but these filters take a long time to design and build (K&L estimated 6 months lead time) so as a compromise, a

[6] As it happens, the amplifier input noise temperature is very close to the sky temperature, and there is enough freedom in the sky temperature within the range of elevation angle to achieve a good balance.

Figure 4.6: Front-end as Built

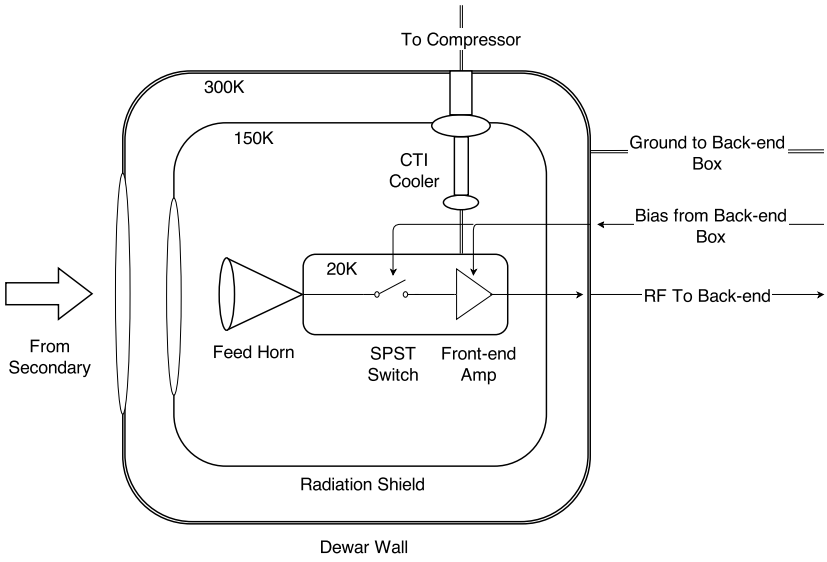

two (identical) relatively narrow band filters from a surplus vendor are used.

Narrowing the band has two effects on the receiver. First, the power is reduced in proportion to the bandwidth and in order to operate within the nominal input power range of the diode a third stage back-end amplifier had to be implemented (see figure 4.7). The second, and more serious effect is the loss of sensitivity (proportional to the inverse-square-root of the bandwidth). The new filter band-width is 5 times narrower than the one originally planned, which gives a temperature uncertainty that is higher by a factor of nearly 2.25.

4.5 The Front-End

The front-end is the section of the receiver responsible for limiting sensitivity. The front-end amplifier temperature sets the minimum receiver temperature. The switch that feeds the front-end amplifier adds to the receiver temperature in proportion to its loss and physical temperature. Any loss in the coaxial transmission lines that

Figure 4.7: Back-end as Built

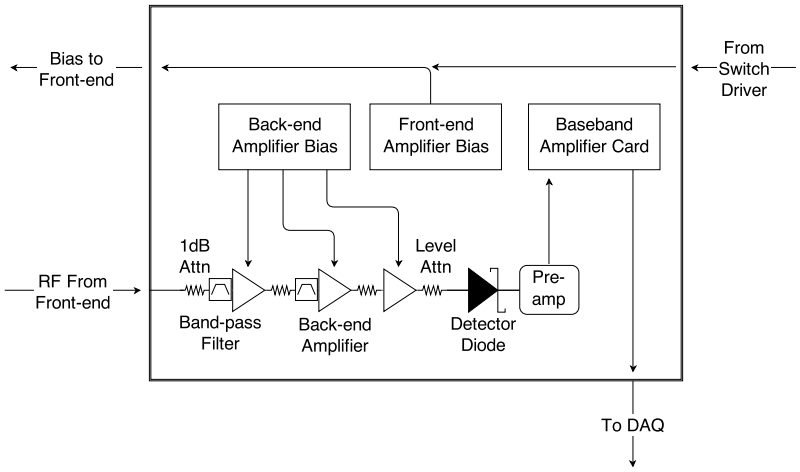

connect the horn to the front-end also contributes, but in general this is quite small ($\sim$ 0.1dB). The main challenge in building a low-noise receiver is in limiting the loss of the switch and the noise temperature of the amplifier.

There are also difficulties involved in cooling the front-end to 20K, where the noise temperature is low. To this end, the entire front-end is housed in a Dewar that reduces thermal loads to a minimum so that the cryo-cooler is not overwhelmed.

4.5.1 Dewar

The Dewar's main job is to thermally isolate the front-end so that it can be effectively cooled. The Dewar is designed to mitigate the three relevant mechanisms of heat transfer (conduction, convection and radiation). This is done by using relatively non-conductive materials where needed, operating the Dewar under vacuum, and shielding the cold parts from thermal radiation.

Since the front-end is rigidly attached to the feed horn, the entire assembly requires

significant mechanical support. Structural G10 tubing is used hold up the horn, while keeping the conduction to a minimum (figure 4.8). Besides this, the only other mechanical connection from the front-end to a warmer stage are the transmission lines that carry the RF signal out of the Dewar and to the back-end. Stainless steel semi-rigid coaxial cable is used for its relatively low thermal conductivity ($\sim$ 6mW for a 4 inch length) and very reasonable RF loss ($\sim$ 0.1dB for the same length)[21]. The standard practice is to strap the coax line to the intermediate stage of the CTI cooler at some appropriate length away from the ambient temperature hermetic connector on the outer dewar wall to reduce the thermal load on the first stage. The CTI cooling power is reflected in figure 4.9.

Air is evacuated from the Dewar using a turbo-pump and roughing vacuum-pump in order to eliminate convection, so the outer shell of the Dewar must be strong enough to withstand atmospheric pressure. Nitrogen, Oxygen, Argon, carbon-dioxide and all of the other significant atmospheric gases with the exception of Helium, which has an atmospheric concentration of about 5 ppm, will have frozen out before the cold-head reaches it's typical low of 20K. This very useful function is known as cryo-pumping, and renders thermal loading from convection almost non-existent.

The outer shell of the Dewar (or the can) (figure 4.10) is built from a single 24 inch diameter, 1/4 inch thick aluminum tube (more than sufficient for 1 atmosphere). This tube adds significant mass to the Dewar, but since the instrument is ground based, this is not a problem. The tube is cut about a third of the way down the length and a vacuum flange is welded onto each of the 4 open ends. The shorter section is modified with two smaller diameter aluminum tubes for the cryo-coolers, welded perpendicular to the symmetry axis, 120° apart at the bottom end of the dewar. The flange at the bottom end of the lower section mates to a flat plate that attaches to the telescope frame. The flange at the top of the longer section of tube

Figure 4.8: Horn and G10 Stand

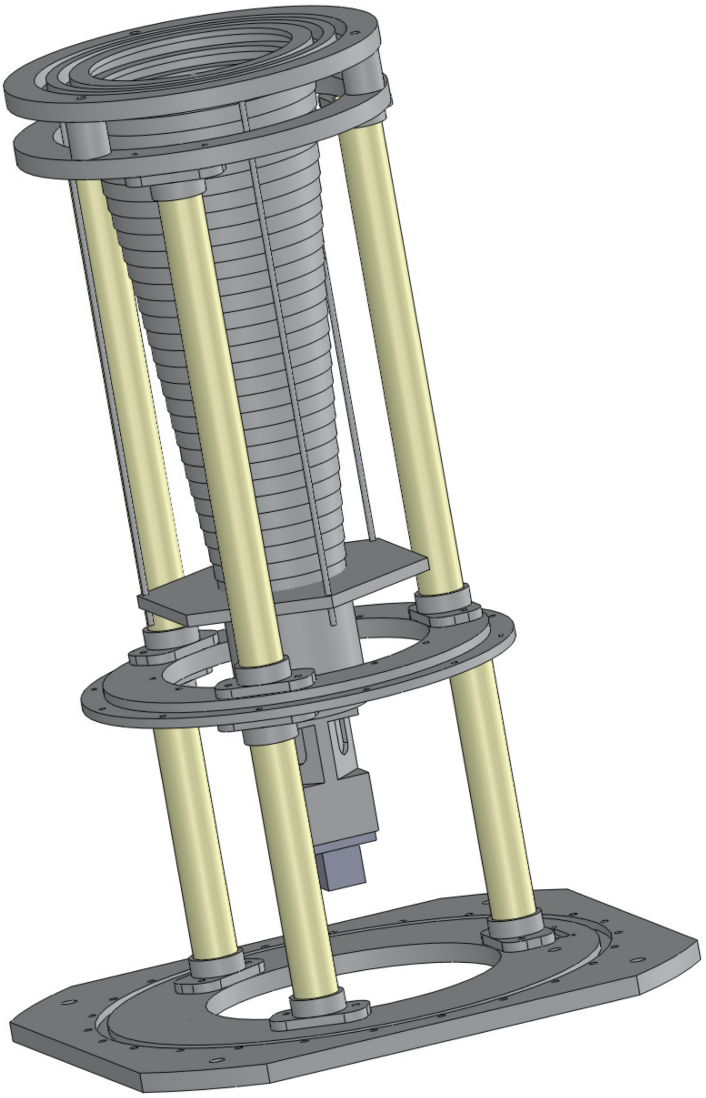

Figure 4.9: CTI 350C Cooling Curves

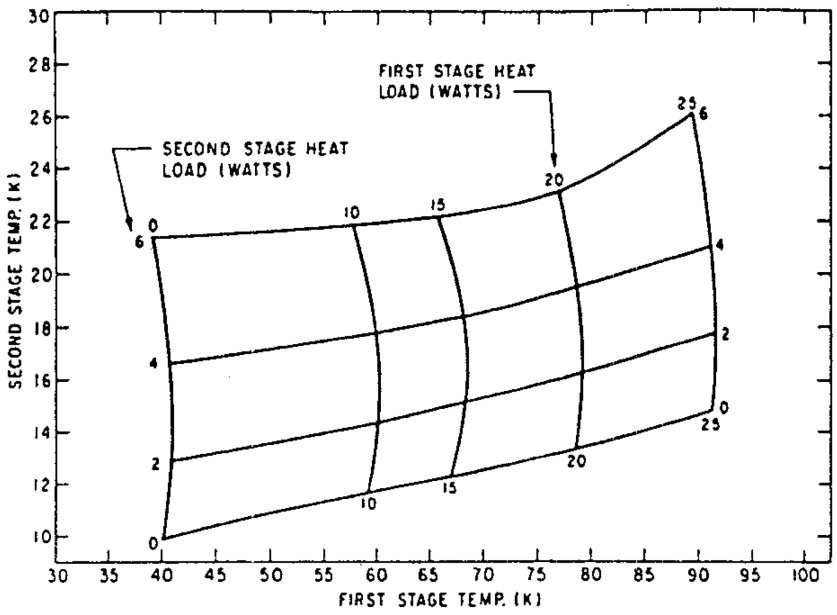

mates to a support ring for the mylar RF window that allows the signal from the secondary mirror to reach the feed horn.

The feed horn and front-end are shielded to keep thermal loading from radiation to a minimum. This Dewar has one inner radiation shield that serves to keep the thermal emission from the 300K aluminum can off of the cold front-end. The top part of the shield is a simple cylinder, with and IR-blocking layered-Teflon window, and the bottom part of the radiation shield has a hexagonal configuration to allow easy attachment to the intermediate stage of the coolers. Several layers of super-insulation (Aluminized mylar) is also used around the shield and the horn to supplement the shielding.

4.5.2 Dicke Switch Options

The types of RF switches considered for the receiver include electro-mechanical, solid-state, MEMS and ferrite. The most important factors considered when deciding

Figure 4.10: Can and Shield

on which switch to employ in the receiver were insertion loss, life cycle (number of switch cycles before failure), and ability to function at cryogenic temperatures. Switching speed is only a concern for amplifiers with a relatively high $1/f$ knee.

Electro-mechanical switches are readily available from a number of RF companies (e.g. Agilent) for a reasonable cost ($\sim$ \$$10^2$). They have the lowest loss for a connectorized assembly (0.5dB is typical) and excellent isolation (90dB), but have very limited life expectancy (a few million cycles) and relatively slow switching speeds (>10ms). They were the last type to be tested cold because it was assumed that they would suffer mechanical failure, and because of their limited life and slow speed. When one was finally cooled it did not fail, so the electro-mechanical switch remains a good candidate for SPDT switch, if only a temporary one.

The solid-state monolithic microwave integrated circuit, or MMIC switches tested include diode and FET switches. The first to be tested was a Hitite (HMC607) GaAs MESFET SPDT switch with a relatively high insertion loss of 1.4dB, but reasonably high isolation (50dB). This switch has a very simple bias network, requiring only simple micro-strip transmission lines to the bond pads, but it failed when cooled to 20K. The next MMIC switch was a MA-COM (MA4AGSW2) PIN diode SPDT switch (figure 4.11). It has reasonable loss (less than 1dB) at room temperature, but requires a more complicated bias tee with DC blocks and RF chokes between the transmission line and the bond pads.[7] It worked when cooled, but the loss doubled to 2dB, possibly due to changes in the diodes I-V characteristics at low temperatures, which could change the impedance resulting in a bad match to the transmission line.[8]

Micro-electromechanical system, or MEMS switches have worked as cryogenic

[7] A concern when using PIN diode switches is distortion due to nonlinear I-V characteristics at high frequencies, but it is not clear what affect such distortion would have on the receiver.

[8] A mismatch would actually cause reflection, not loss, which is not as bad as real loss since it doesn't add to the noise power.

Figure 4.11: MA-COM SPDT PIN Diode Switch

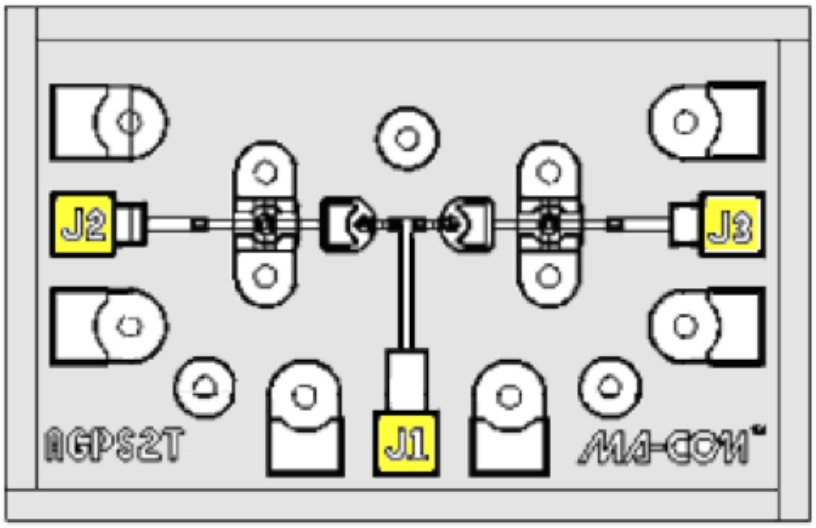

Yellow areas indicate bond pads

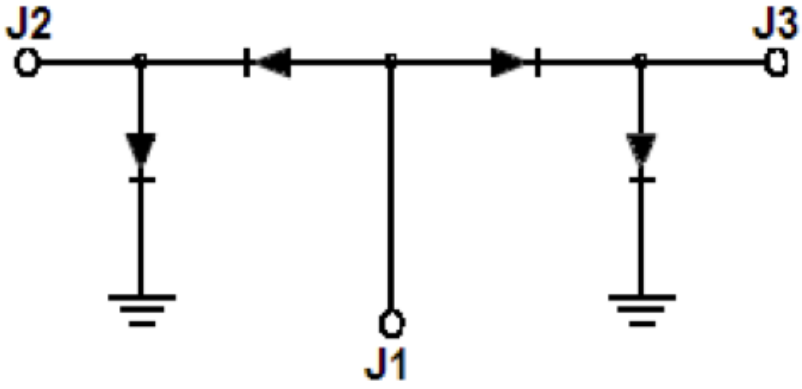

switches in radio receivers in the past. The company that produced the previous generation of working cryogenic MEMS switches has since gone out of business, but a switch from a comparable company was tested. The Radant RMSW221 (figure 4.12) have good insertion loss (<0.25dB at 10GHz) and reasonable isolation (20dB), a life cycle count over 10 billion and very good switching speed (<10us). For these reasons MEMS switches are the most attractive type of switch for the receiver front-end, but this particular switch failed when cooled. The failure mechanism is believed to be freezing of gas inside of the cap that protects the MEMS device. The switch functions normally after being warmed from cryogenic temperatures, which seems to rule out mechanical damage. One solution to the freezing gas problem might be to release the gas from the cap. This was done and when tested the switch worked in atmosphere for a few seconds before degrading. It might be possible to operate this switch without the protective cap since the switch would be used exclusively in vacuum, but this has not yet been attempted.

Waveguide and coax ferrite switches operate on the same principle as waveguide circulators and isolators, but use temporary magnets magnetized by solenoid current pulses to switch the direction of circulation. Cryogenic front-end ferrite switches were used in ARCADE, and waveguide circulators with <0.5dB loss at 10GHz are readily available, but building a cryogenic ferrite waveguide switch is not a trivial matter and only one individual (in Russia) was found who could build such a device[9]. Given a design and bill of materials such a switch could be manufactured relatively cheaply, but as of this point no such design is available. Coaxial ferrite switches are also a good possibility, and would be easier to implement than a waveguide switch, but these are also unavailable commercially.

Given that only one of the types of switches tested actually worked, it was

[9]His estimated lead time was 9 months

Figure 4.12: Radant MEMS Switch

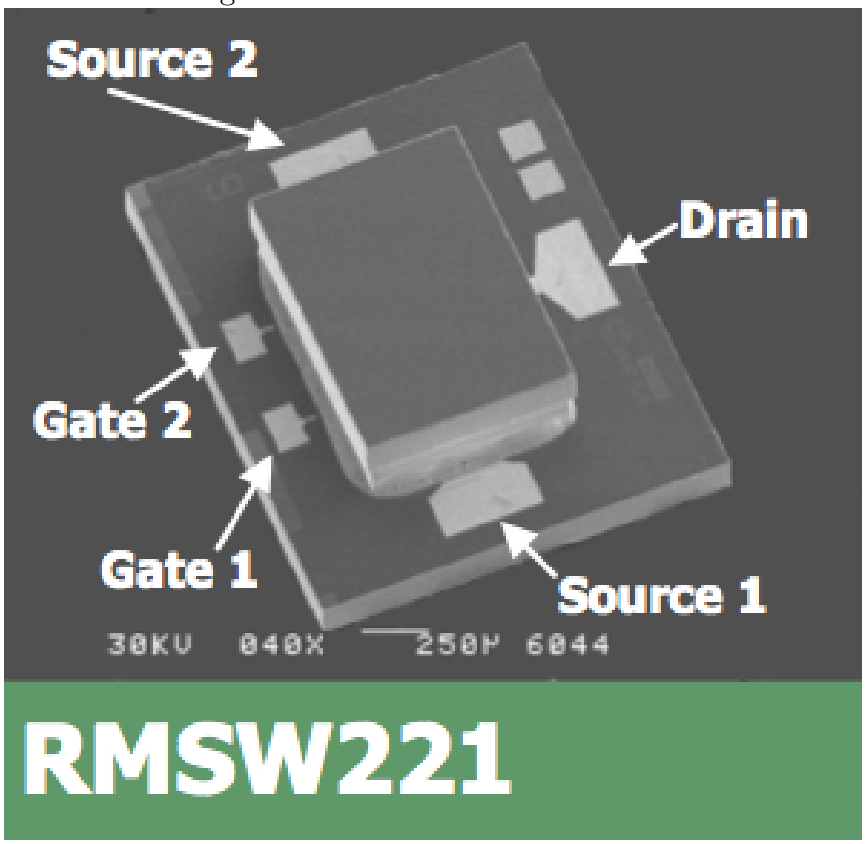

reasonable to investigate variations of that type to look for a better alternative. MACOM makes a SPST reflective switch (MA4AGSW1) that uses the same technology as the SPDT, but instead of the PIN diodes forming the transmission line itself, they only serve as a ground connection off of the transmission line that is either shorted or open (figure 4.13). This small difference in the design means that any mismatch in the PIN diode would only effect isolation and not transmission. Testing this switch showed that the loss was unaffected by the temperature change and that the isolation was acceptable (20dB) when cooled. As already mentioned, choosing this switch meant rethinking the way the receiver operates and in the end led to a simpler overall design.

The MA4AGSW1 also have a remarkably low loss of ~ 0.1dB on chip. The best connectorized assembly has a loss of ~ 0.5dB, but this assembly failed when cooled. The existing reliable assemblies have a loss closer to ~ 0.8dB.

4.5.3 Switch Assembly

The switch housing is built on a gold plated[10] machined brass body with cavities for the transmission lines and bias tees as well as bias connections (figure 4.14). Each brass body was cut on a small custom-built CNC milling machine. The assembly includes the MMIC chip itself ($\sim$ \$25 each), transmission lines and bias tees, a bias connector, off the shelf SMA connectors and a lid.

As an aside, two custom built CNCs machines were used in the fabrication of the in-house MMIC housings. Each of them are fitted with linear micron encoders for increased temperature stability over the more standard rotary encoders for measuring stage position.[11] Tooling for the PIN diode switch housing included end mills from

[10]Gold plating took place at either Hudson Plating works or Electronic Precision Specialties Inc.
[11]The high accuracy of the smaller milling machine and its high performance NSK spindle made it

Figure 4.13: MA-COM SPST PIN Diode Switch

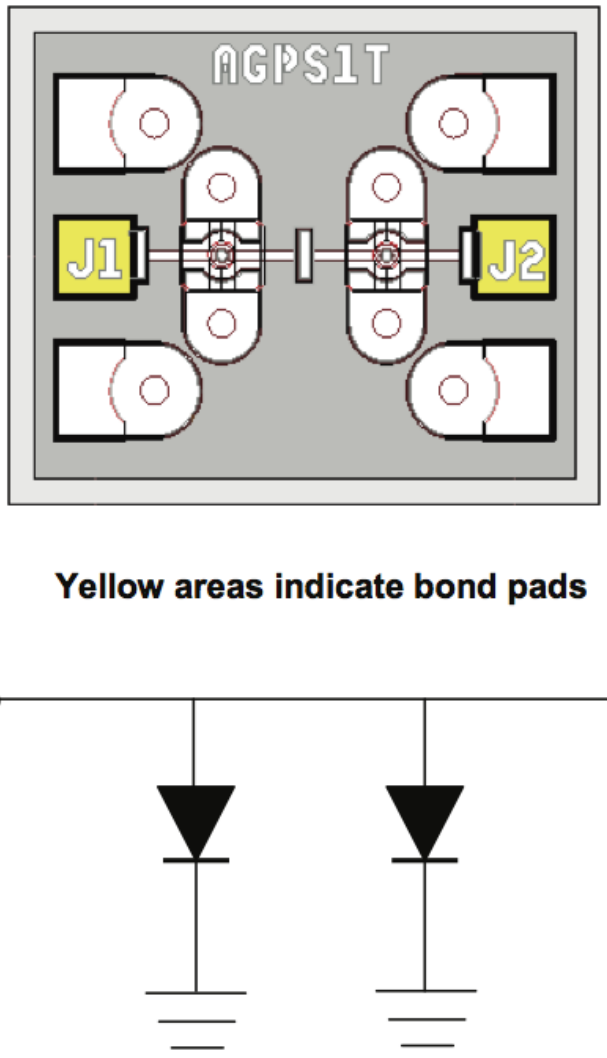

Figure 4.14: Gold Plated Brass Housing

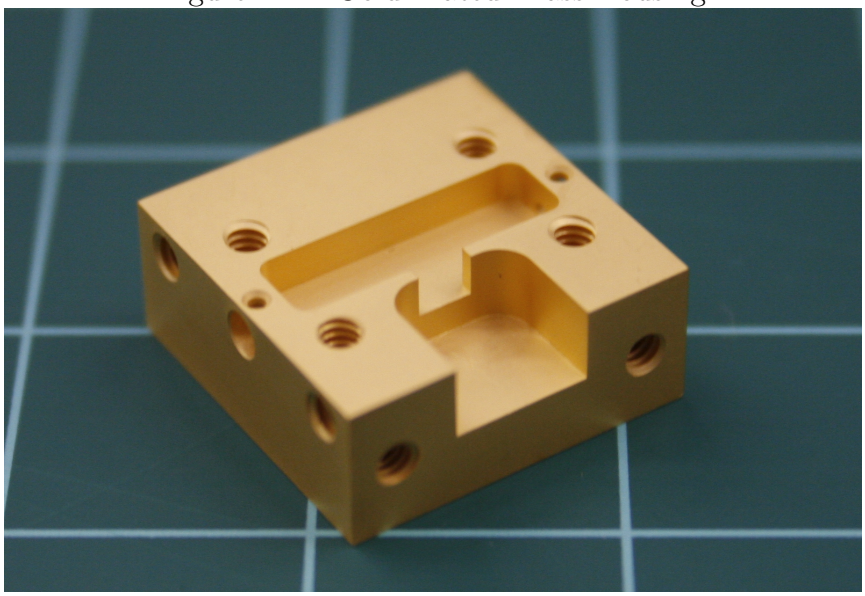

from 1/8 inch down to 3/64 (all standard sizes).

The small scale and high precision of the mill made it possible to machine circuits as well. The small circuit boards to which the bias connectors are soldered were machined into copper-clad FR4 with very reliable results. Machining onto softer substrates such as Teflon used in the transmission lines and bias tees proved less effective, and those components had to be etched in usual way using a mask (figure 4.15), photo-resist and a copper etching compound (in this case Ferric-chloride). The mask has a number of micro-strip transmission lines with a single strip as well as two different sized bias tees that have a narrow strip with two or three right turns in it.[12] The broader straight lines that come off perpendicular to the transmission line are there for electrical an connection during gold plating and are removed prior to assembly.

possible to produce a large number of W-Band waveguide amplifier housings, as well as a variety of associated waveguide components for use at JPL. Tooling for these parts include end mills ranging in diameters from 1/8 inch down to 0.004 inch.

[12]These are actually just RF chokes and don't include DC blocks. It turned out that DC blocks were unnecessary as the coax transition on the input to the switch is not connected to ground, and the front-end amplifier input has a DC blocking capacitor built in.

Figure 4.15: Mask for Etching Bias Tees and Transmission Lines

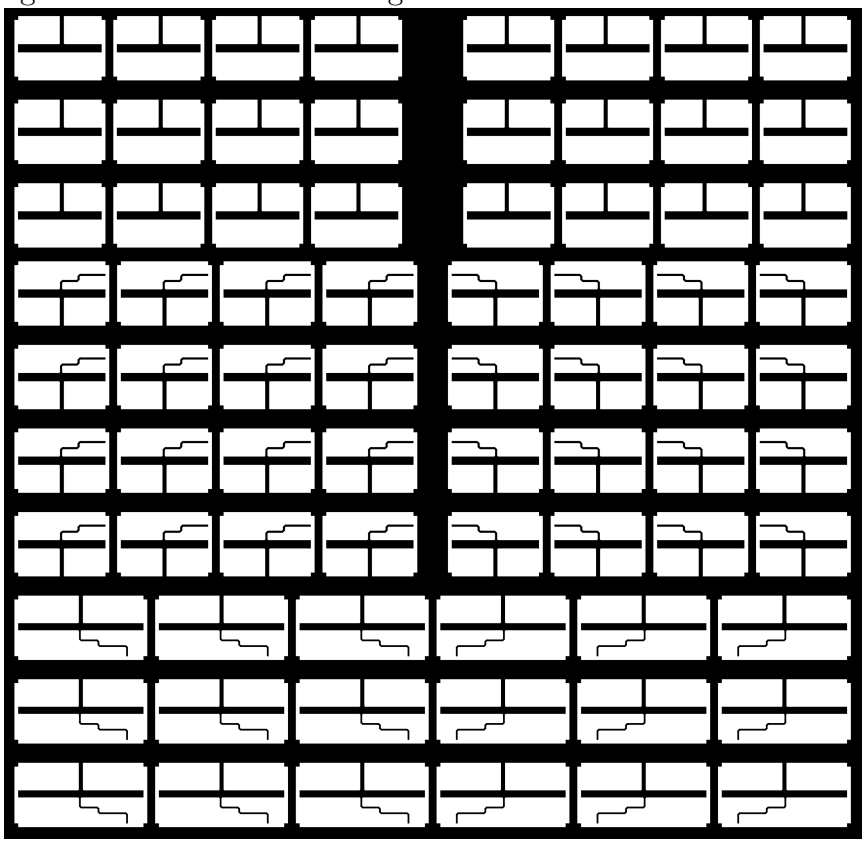

The transmission line and bias tee designs were taken from a basic bias tee concept and developed using the Sonnet microwave studio software package. They were optimized parametrically for the SPDT switch housing (very similar to the SPST housing), so they had to be modified slightly to fit.

The assembly process begins by soldering the bias circuit board and connector as well as the glass bead RF feed-throughs into a bare housing. This is done using a standard 60/40 Lead/Tin solder with a melting point of 188°C. Then, after carefully cutting out the bias tees and transmission lines using a scalpel and straight-edge, they are soldered, along with the MMIC chip into the RF cavity of the brass body using an alloy of 58/42 Bi/Sn (Indium corporation Indalloy #281) with melting point of 138°C. The glass bead feed-through pins are soldered onto the transmission lines using a 52/48 In/Sn (Indalloy #281) alloy with a melting point of 118°C. The alloys with lower melting temperature are used to avoid exposing the MMIC to high temperatures which could be damaging, and are chosen to be soft metals that can absorb some of the strain from differential CTEs during cooling. The reason for using two different low temperature alloys is that the Bismuth alloy has a melting point above the temperature required to achieve good wire bonds, while the Indium alloy has a melting point a little below bonding temperature. Also, Bismuth does very well between two flat surfaces and is used between the ground planes of the MMIC and transmission lines and the housing, whereas the Indium is softer and forms a more reliable connection between the feed-through pin and the top of the transmission line.

After all of the parts are soldered in place, the transmission lines are wire-bonded (using 1mil gold wire) to the pads on the chip to complete the RF circuit. The bias circuit board trace is bonded to a 100pF grounding capacitor, then the capacitor to the end of the bias tees RF choke.[13] The lid, the bias connector strain-relief strap

[13]The grounding capacitor and the bond to the RF choke form part of the RF circuit. A short

and the SMA connectors are bolted onto the body to complete the assembly.

The particular choice of process and solder were reached after observing several mechanical failures while cooling to cryogenic temperatures. The most common failure mode was wire bonds that were made too short pulling loose. The other common failure point was the solder connection between the chip and the housing. After some practice it became possible to put together reliable cryogenic switch assemblies.

4.5.4 The Front-end Amplifier

The front-end amplifier is an InP HEMT amplifier designed by Sander Weinreb of CalTech. It is among the lowest noise amplifiers available in this frequency range, and was purchased for a few$\times\$10^3$. The package uses SMA connectors for ease of use and a protective bias network to help avoid electrical damage (though special care is always taken to avoid static discharge onto the bias pins). The amplifier was provided with recommended bias voltages that maximize gain and minimize the noise temperature at both 300K and 20K (figure 4.17 shows the cold bias).

At the optimal bias point the noise temperature is 5K up to almost 11GHz and the gain is close to 40dB and relatively flat across the 7 to 11GHz band. The outstanding noise figure means that even with a modest 500MHz pass-band the radiometer could measure temperature with a sensitivity[14] of $448\mu\mathrm{K}/\sqrt{\mathrm{s}}$, making it more sensitive than the WMAP (4GHz wide) K-band radiometer [18], and the high front-end gain makes it relatively insensitive to noise in later gain stages.

It has a 1dB compression point (where the output power is $\sim 20\%$ below the expected linear output) at -40dBm of input power, or about 100nW. For comparison, a 1W (EIRP) radio transmitter would need to be just under 1km away to compress

bond, while improving the RF performance, is subject to mechanical strain when cooled due to the different expansion coefficients of the Teflon substrate and capacitor dielectric material.

[14]This includes the factor of 2 increase from chopping.

Figure 4.16: X-Band LNA Housing

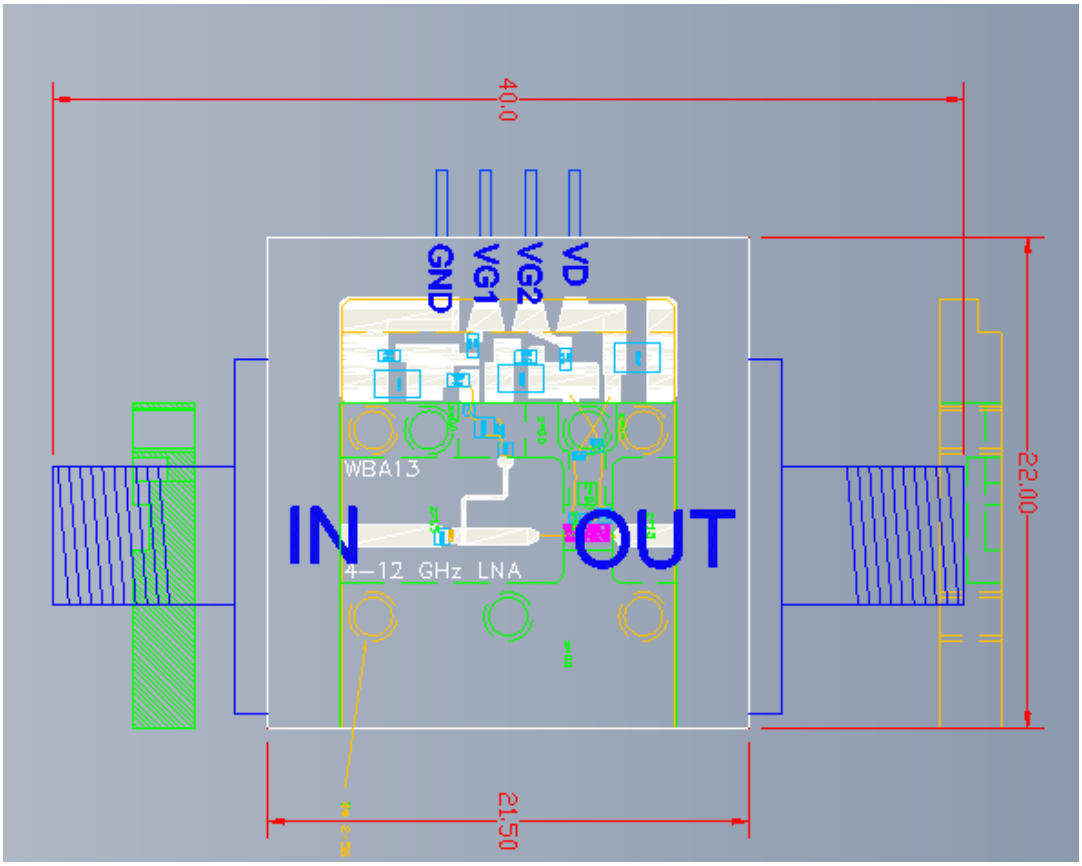

Figure 4.17: Front-end Amplifier Bias Recommendations and S-Parameters

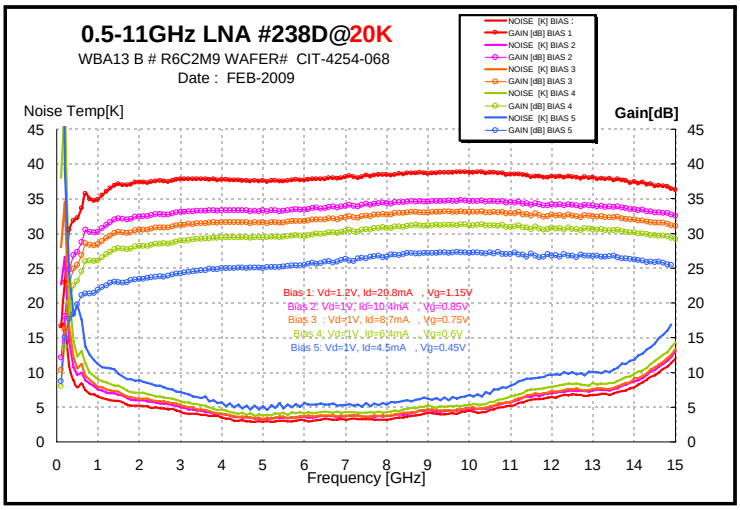

the front end by 1dB if the telescope beam was directed toward it[15]. The power from the sun is not even close, with only about 2pW of input power (assuming a 2° beam), about the same as a beam filling blackbody.

The current draw is dominated by the drain current ($\sim$ 20mA at 1.2V) and puts relatively little thermal load on the cooler. The gate current draw is negligible ($\sim 300\mu$A, most of which is dissipated in the bias network).

4.6 The Back-end Box

The back-end box contains the warm back-end of the receiver and since it is convenient to keep the bias and readout electronics close to the receiver they are housed in the back-end box as well. The box itself is (mechanically and electrically[16]) attached

[15]Assuming a source EIRP of 1W at a distance of 1km, a 1m^2 primary would collect 80nW.

[16]It is important to note that the RF ground, shared by the front-end and back-end receiver components, is connected to the dewar and back-end box case through the hermetic RF connectors,

to the dewar and connects to the front-end through hermetic baseband and RF connectors.

One major role that the enclosure provides is protection from RFI. While all of the coaxial transmission lines are shielded from RFI contamination, the back-end amplifiers are relatively exposed. The bias electronics for all of the amplifiers are housed in the back-end box, and could conceivably introduce RFI into all of the gain stages through the bias wires. This is avoided by the use of so-called pi-filters on every electrical connection into or out of the box and careful attention is paid to ensuring an RFI proof enclosure.

The other role of the back-end box is to insulate the RF and baseband components from temperature changes that can lead to significant gain drifts. The eventual goal is to have the entire back-end box temperature stabilized, but this has yet to be implemented.

4.6.1 Back-end Amplifier Noise and Gain

The RF back end has three gain stages, each with about 21dB of gain in the band between 6GHz and 12GHz. The gain is provided by commercial MMIC amplifiers (United Monolithic Semiconductors part number CHA3666). The chips are packaged in the same brass housings used for the SPST switch housings.[17]

The CH3666 is reported to have a noise figure of 1.8 in the band around 9GHz corresponding to a noise temperature of nearly 150K.

$$T_{Noise} = 290(10^{\frac{NF}{10}} - 1) \tag{4.1}$$

the CTI cooler head, and the bias electronics ground.

[17]This body design is based on a combination of the amplifier housing design used by Weinreb for the front-end amplifiers and the one used in the BEAST receiver.

This is an acceptable noise temperature for the second and subsequent gain stages because of the high front end gain of 38dB (about x6000). The front-end receiver noise temperature is amplified by the front end gain before the first back end stage adds any noise, so the effective noise contribution from the first back end stage is an almost negligible $\sim$ 25mK.

The 1dB compression point is given at an output power of 17dBm, or about 50mW. Since there is so much gain in the RF chain, it is important to make sure that the last stage RF amplifier gain does not compress at all.[18] The theoretical input power from a blackbody at room temperature is

$$P = kT\beta \approx 2\text{pW} \tag{4.2}$$

where $k \approx 1.38 \times 10^{-23}\text{J} \cdot \text{K}^{-1}$, is Boltzmann's constant, $T = 290\text{K}$ is room temperature and $\beta = 5 \times 10^{8}\text{Hz}$ is the filter bandpass. The predicted output power of the receiver, after all of the RF gain stages ($\sim$ 90dB including attenuation added before the last stage) is 2mW, safely below the 1dB compression point, so only compression from RFI power is of concern. Compression from RFI sources in the band would be a secondary problem, but out-of-band RFI could be a problem.

The figures that are provided in the specs sheet are the IP3, the 3rd order intercept point, and C/I3, the ratio of the carrier power to the third order intermodulation power. The specs sheet for the CHA3666 has plots of IP3 and C/I3 vs output power (figures 4.18 and 4.19). The IP3, the output power for which the 3rd order intermodulation signal power would be equal, has a value between 26 and 27dBm for values of output power, at 8GHz, from 1dBm up to about 10dBm, after which it starts to roll off. The C/I3 drops linearly from 1 to 10dBm, after which it too rolls

[18] Any gain compression, however minor, would have a dramatic effect on the receiver output.

Figure 4.18: CHA3666 C/I3

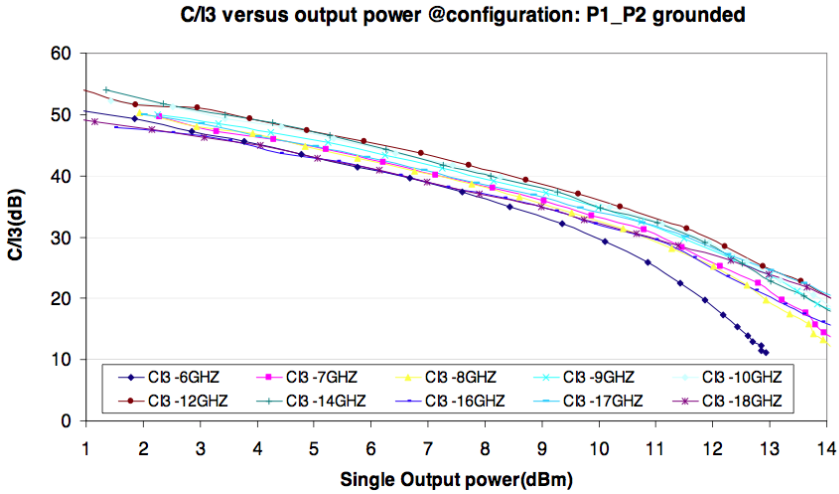

off. If these are used as benchmarks of good or normal performance, the amplifier would appear to be reliable up to 10dBm of output power and there is no need to question the gain linearity at the few dBm level.

The back-end chain has one band-pass filter on the input, then two gain stages, followed by another filter and another gain stage before the leveling attenuator and detector diode. This configuration is designed to minimize the gain on out-of-band RFI. Still, the actual amplifier compression was never tested, and even though it seems unlikely that there is enough RFI power around to cause compression is can't be completely ruled out.[19]

4.6.2 Back end amplifier assembly

The design of the housing is actually a hybrid of the front end amplifier housing designed by Hamdi Mani in collaboration with Sander Weinreb, and the housing for the BEAST front end. The main features are an RF cavity stretching from one side wall to the other and a cavity that opens to the outside for the bias connector.

[19]Some data taken with the back-end box lid removed appeared to suffer from compression.

Figure 4.19: CHA3666 IP3

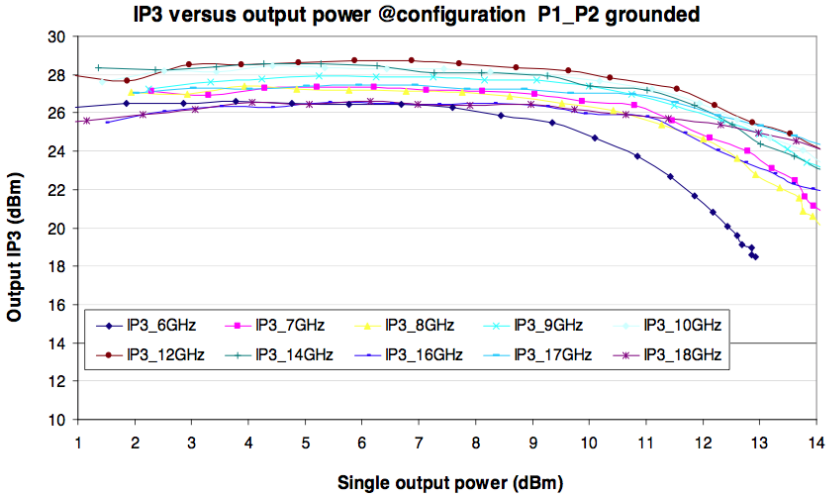

There is an opening on one side of the RF cavity where the wire bonds from the bias connector enter. At either end of the RF cavity there is a small hole where a glass bead feed-through connects the transmission lines to the SMA connectors bolted onto the outside.

Signals enters the RF cavity by way of the glass bead feed-throughs. The feed-throughs are a short coaxial transition with a gold plated pin center conductor, a glass insulating cylinder and a thin gold plated outer conductor. The outer conductor is soldered into the body using standard 60/40 Sn/Pb solder (Melting temperature 188°C). Since the back-end amplifiers are operated at room temperature, the transmission lines, the chip and the bonding capacitor are attached to the ground plane using a conducting, silver epoxy(EPO-TEK H20E).

To complete the RF circuit the feed-through center conductor is epoxied to one end of the transmission line and the other end of the transmission line is bonded directly on the amplifier chip[20]. The wire bonds that connect to the amplifier bias pads originate on 100pF bonding capacitors (American Technical Ceramics part

[20]This is done using 3 bonds since the available wire bonder uses 1mil gold wire not ribbon, to help reduce loss

number: 111SK101M100TT). These capacitors serve as an RF ground to help keep RFI and noise off of the chip, but also help mechanically by providing a convenient means of making the wire bond connections from the bias connector to the chip.

4.6.3 Detector Diode

The detector diode converts the RF power to a DC voltage that can be recorded by an ADC (analog to digital converter). The detector diode is an HP (now Agilent) low barrier Schottky diode square law detector. The Schottky diode is used for the low voltage drop which allows for high sensitivity without biasing, and its faster switching speed which makes it suitable for GHz applications. A typical detector diode will output 1mV per μW.

The detector is operated in the square-law part of it I-V curve, but its power response is significantly non-linear when operated over a large power range. Figure 4.20 shows the deviation away from purely linear response (fit at power below 1mV). It is clear that compression becomes significant (about 5%) at just 5mV. Figure 4.21 shows the same data plotted in a log scale to show dB of compression. In order to keep the diode output voltage in the most responsive range, the input power is reduced by a leveling attenuator (currently 6dB) to keep the peak diode output voltage below a few millivolts.

The variations in the output voltage due to differences in the source temperature are in the tens of microvolts, so the diode response is actually very linear for measurements in a relatively small power range. The non-linear diode response is most noticeable in measurements that require a large dynamic range. Y-factor measurements in which the input power range is an order of magnitude are particularly sensitive to diode compression.

Figure 4.20: Agilent Voltage Output vs. Input Power

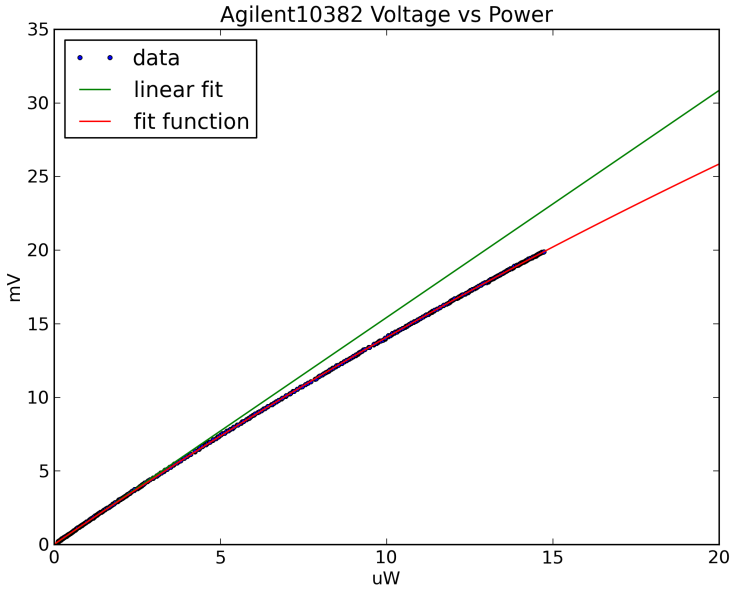

Figure 4.21: Agilent Compression vs. Input Power

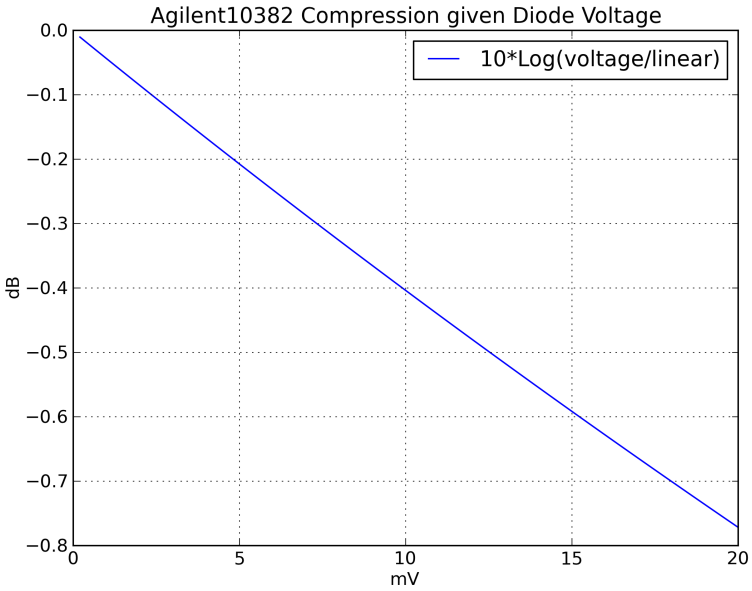

4.6.4 Analog and Digital

During normal operation the output of the DC component of the detector diode is kept to around a millivolt. This is already a small signal to measure with a voltmeter or ADC, but as mentioned, the interesting variations in the average DC level are only on the order of tens of microvolts. This small signal must undergo a few stages of gain and filtering before it can be recorded by the DAQ.

In order record all of the information in the data, the ADC must have a resolution much better than the noise level at a few microvolts. The data acquisition system used is an IOTech (DaqBoard3000USB) 16 bit DAQ with a few counts RMS[21], each of which correspond to about $\sim 300\mu$V in the $\pm$10V range. This sets the minimum baseband gain required at a few thousand. This is done in two stages.

The pre-amp provides a gain of x100 and is connected directly to the diode output to help reduce noise. The pre-amp also provides a 600Ohm load on the output of the diode. The pre-amp output is send to a second amplifier, located on a board adjacent to the amplifier bias boards. This board incorporates a Sallen-Key low-pass filter with a roll-off frequency set to 300Hz. It performs what is essentially a rolling average of the diode output so that the signal can be recorded at a reasonable data rate, chosen to be 10kHz to allow for some oversampling. After the low-pass filter, the signal is passed low frequency high-pass filter to remove the DC component before further amplification. The second stage gain is x300, for an overall post-detection gain of x30,000.

After the data is recorded by the DAQ it is ready for post-processing, which is discussed in the next chapter.

[21]This can be greatly reduced by oversampling, up to the maximum aggregate sampling rate of 1MHz.

Chapter 5

Data

Santa Barbara is by no means ideal for conducting sensitive radio measurements. As discussed in the chapter on RFI, the radio spectrum is full of very bright sources that could interfere with the signals of interest. Still, with the aggressive filters that have been implemented it is possible to remove RFI a to sufficient degree to allow deep integrations on the sky. But there is another serious factor that limits sensitivity to extraterrestrial sources at 9GHz, namely water vapor. The climate at UCSB in particular is very humid and, for large fractions of the time, foggy. There is an undeniable fact that even on clear days water vapor interferes to such an extent that scientific data is largely unattainable.

5.1 Receiver Temperature

Before investigating the possible sources of interference, it is important look at is receiver sensitivity. The band pass filter chosen to block RFI only has a 500MHz wide pass band. This limits the sensitivity compared to the original receiver design, which had a band pass filter 2.4GHz wide. Another major factor affecting the receiver

sensitivity is the front end switch that modulates the signal before it sees the front end amplifier. The band pass filter affects the sensitivity, but the switch loss, along with the front end amplifier noise temperature determine the receiver temperature T_{rec}. Receiver temperature is equal to the antenna temperature needed to double the receiver output.

$$T_{rec} = \frac{1}{e}(T_{amp} + T_{phys}(1 - e)) \tag{5.1}$$

where e is the transmission efficiency of the switch (as in Kraus [16]), T_{amp} is the amplifier noise temperature and T_{phys} is the physical temperature of the lossy element (the switch in this case). The switch chip was chosen to be very low loss (see switch section) and the initial assembly had about 0.5dB of loss. After several thermal cycles the chip ground plane became separated from the housing and needed repair. After the repair process the chip had a loss closer to 0.8dB giving the efficiency a value of about 83 percent. The amplifier noise temperature is given to be about 5K and the physical temperature of the lossy switch is about 20K, so the overall predicted receiver temperature is 10K (with a 0.5dB loss switch it would be 8K).

The receiver temperature is measured using the y-factor method at two known antenna temperatures. This is done using Eccosorb, which is the trade name for a material with very high emissivity (and absorptivity) at microwave frequencies. A y-factor measurement was done with the receiver on the telescope frame with the horn oriented in a horizontal direction. (In this orientation the telescope beam point to a relatively low elevation.) The absorber was placed in a Styrofoam cooler directly in front of the dewar window to completely fill the beam. Measurements were taken on the absorber at room temperature and after it was cooled with liquid nitrogen. A reference measurement was also taken on the low elevation sky. Each measurement

was taken for 1 minute to allow for a power spectrum with reasonable resolution.

One way to calculate the receiver temperature is to use the pre-amp output voltage. After accounting for the offset voltage in the back end electronics and dividing by the preamp gain (x100),[1] the diode output voltages were found to be 27.7mV at room temperature and 10.25mV when cooled, which gives y-factor of 2.8 (Figure 5.1). Assuming a warm target temperature of 300K and cool target temperature of 77K the corresponding receiver temperature is 54K. This is far above the expected value, and seems very unlikely. The ratio of the diode voltage on the warm target to that on the sky is just above 6. Assuming that the receiver temperature really is 54K, the system temperature ($T_{sys} = T_{ant} + T_{rec}$) on a warm target would be 354K,[2] which puts the system temperature on the low elevation sky at about 58K. This suggests a sky temperature of only 4K, which is far too low for the Santa Barbara sky even at zenith.

One potential cause for the error in y-factor is that the cool temperature was above 77K.[3] Another possible cause for a high receiver temperature is an error in the offset voltage, but these were measured carefully. The most obvious source of error is diode compression. Data taken on the diode suggests that a diode output voltage of 10mV is compressed by .4dB, and at 27.7mV compression is about 1dB (from extrapolation). Taking the compression into account gives a new y-factor of 3.1 and receiver temperature of 29K. This is still higher than expected.[4]

Another way to measure receiver temperature is to look at the power spectra. The

[1] This is related to the amplifier bias current and has a value of about +30mV.

[2] The receiver temperature is defined with a factor $1/e$ in front to allow the system temperature to be the sum of the receiver temperature and antenna temperature without having to scale the antenna temperature.

[3] The Eccosorb is cooled in a plastic bag filled with liquid nitrogen. The bag was inside of Styrofoam box, but opaque frost could have developed on the bag.

[4] Taking compression into account these figures gives an adjusted voltage ratio of 7.4 between a 300K target (with 329K system temperature) and the low elevation sky, suggesting a low elevation sky temperature of 15K.

Figure 5.1: Plot of diode voltage at 3 Antenna Temps

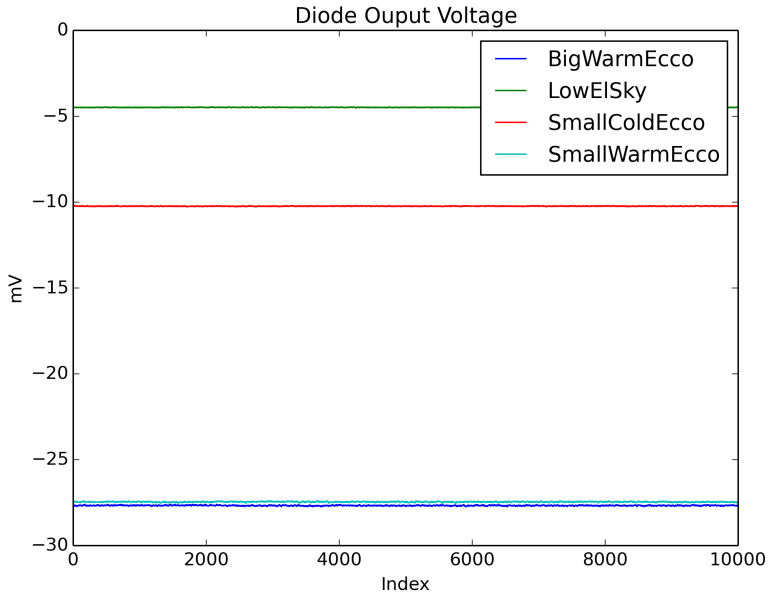

spectral power is proportional to the system temperature, so the y-factor can just as easily be found using the white noise levels. Figure 5.2 shows the power spectra of the same diode voltage measurements in Figure 5.1. The data from used to make the spectra has an additional baseband (AC) gain stage (x300), so the voltages are divided by this as well as the pre-amp gain. The power spectrum has the benefit of being unaffected by the DC offset. The ratio of the white noise levels of the warm and cool measurements is around 3 as expected.[5] The ratio of the warm and sky noise levels also agrees with the DC voltages.

The resolution of the spectrum can be determined by the number of data points used to calculate the FFT (NFFT) and the sample rate. The sample rate is 10kHz and the number of points per FFT block is 2^{12} so the spectrum resolution is a about 2.5Hz.[6] The label on the y-axis in Figure 5.2 is μV/BW. It is necessary to take the

[5]The white noise level is taken below 150Hz, where the effect of the 300Hz roll-off due to the low pass filter in the back end is negligible.

[6]All of the data here was taken at this sample rate. According to the sampling theorem, a

Figure 5.2: Log Plot of PSD at 3 Antenna Temps and Receiver Off

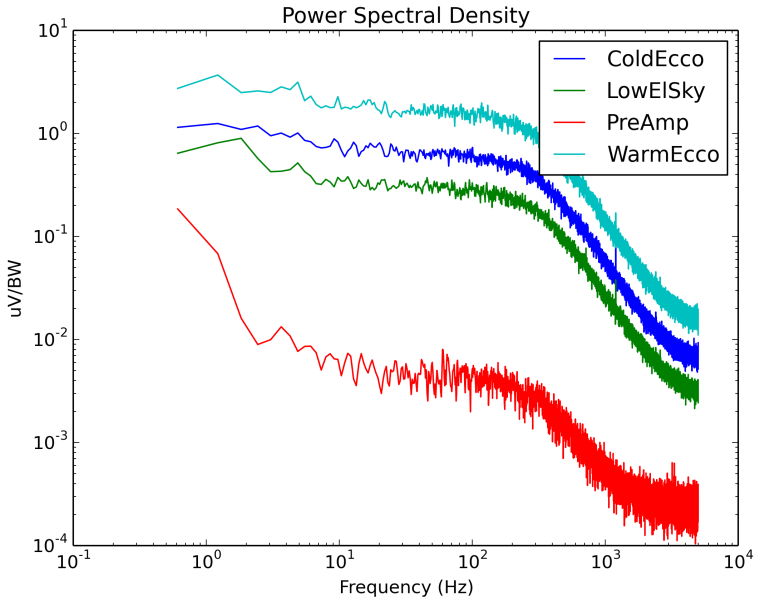

square root of the diode voltage power because calculating Python's matplotlib.mlab psd function squares the FFT to find the power, but the voltage out of the detector diode is already proportional to the power, so this spectrum is actually the amplitude spectral density of the diode voltage, but is proportional to power.

It is useful to work in units of volts (or μV) out of the diode to compare the noise power to the equivalent input voltage noise of the pre-amp of $\sim 4\text{nV} \cdot \text{Hz}^{-1/2}$. The pre-amp noise is visible in the figure and agrees with the given value. The white noise level of the sky measurement is $\sim 300\text{nV/BW}$ so the contribution is only a couple of percent.[7] The diode noise is given as $< 50\mu$V at high input power[8] and is probably a gross overestimate at low power, but working with such a low detector diode output voltage is not a good idea.

sample rate of 10kHz puts the highest frequency spectrum component at 5kHz. The figure shows the truncated spectrum.

[7]The units look different but are equivalent since the spectrum bandwidth is 1Hz

[8]This is as measured for a CW input power that produces a 100mV output voltage (the response is $\sim 1\text{mV}/\mu\text{W}$).

The y-factor measurements were taken with added attenuation (a 6dB attenuator was used) to prevent excessive diode compression during measurement of the warm target. After completing the y-factor measurements the attenuation was reduced (to 1dB) to bring the voltage on the sky to a reasonable level, and the voltage measured again to provide a good comparison. The ratio of the diode voltage measured on the low elevation sky with the 1dB attenuator and the 6dB attenuator is just over 3, and corresponds to a gain of 4.86dB, close to the expected change in attenuation of 5dB.

5.1.1 Zenith Temperature

Another check on the receiver temperature, besides the y-factor measurement, is the sky dip (figure 5.3).[9] This is a data set of the diode voltage (with a 1dB leveling attenuator) during a scan in elevation angle. The diode voltage close to zenith is just over 7mV, the ratio of the warm target (adjusted) voltage to the zenith voltage is 23.2, and taking the system temperature on the warm target at 329K gives a zenith system temperature of 14.2K, clearly in conflict with the the 29K receiver temperature found above.

Assuming a receiver temperature of 10K (and a warm target system temperature of 310K), and taking the ratio again suggests a zenith temperature of just over 3K. This is again far too low for the Santa Barbara Sky, and could indicate that the diode compression was overestimated. Either way it appears that the system temperature is less than 29K. Taking the receiver temperature to (somewhat arbitrarily) be 20K and factoring in the change in attenuation it is possible to estimate the conversion factor from voltage to temperature to be 3.8K/mV.

[9]The elevation angle is not well known and attempts prevented a successful fit to the data.

Figure 5.3: Plot of Diode Voltage vs Elevation Angle

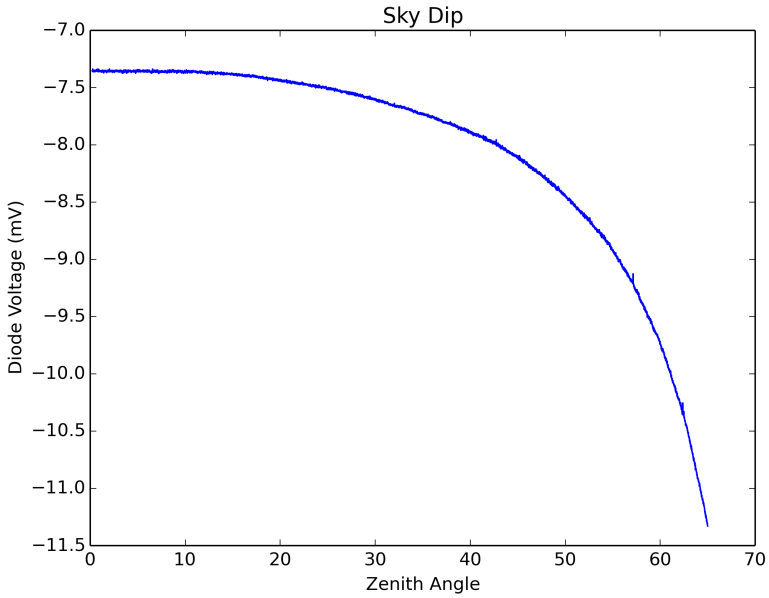

5.1.2 The Moon

One last way to check the temperature is the moon. One of the data sets discussed later contains several scans of the moon. The scan of the peak is shown in figure 5.4, with relative diode voltage compared to the reference load. The telescope beam FWHM (full width at half max) can be approximated by the width (at half max) of the scan minus the width of the moon ($1.9° - 0.5° = 1.4°$), so a rough estimate of the moons filling factor of 13%.[10] Taking the average lunar surface temperature at 235K gives an expected antenna temperature of 30K.

Since this is a relative measurement, it can be used to find a ratio between voltage and temperature, but it is also important to know the diode levels. Figure 5.5 shows the un-demodulated moon scan data. The background sky level is 8mV and the peak moon voltage is 14mV.[11] Including a diode compression of 0.4dB, this gives

[10]The beam area is approximated as the area of a circle of radius FWHM/2. The moon area is calculated in the same way and the ratio is taken.

[11]An interesting detail here is the increase in the load temperature during the moon crossing. It

Figure 5.4: Plot of Single Scan Across the Moon

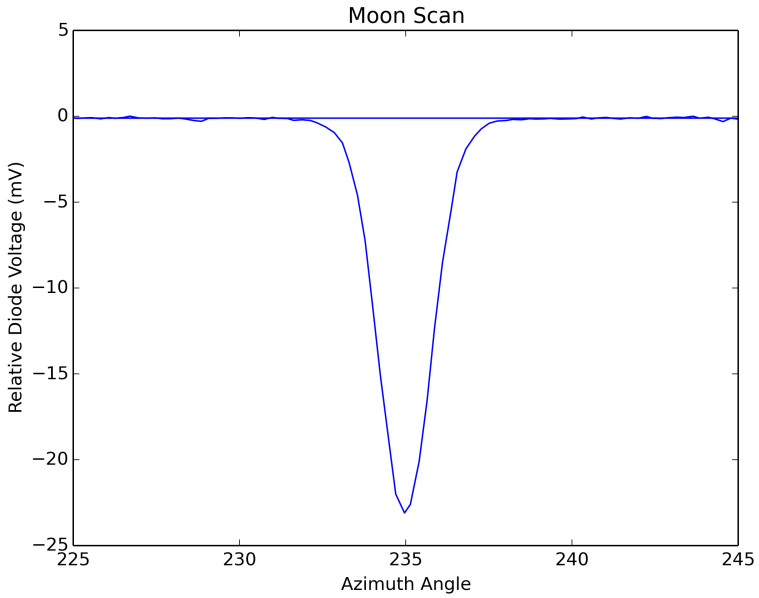

a conversion factor of 4.56K/mV, and suggests a system temperature on the sky of 36.5K.[12] This is most likely an overestimate given the way the beam size was determined.

5.2 $1/f$ Noise

In the plot of the power spectrum in Figure 5.2 the low frequency feature that rises above the white noise level is obscured by the course resolution. In order to get better frequency resolution and more FFT blocks to average together, much longer data sets are required. The sky data plotted in Figure 5.6 was taken for a period of 50 minutes looking at the sky (to the east) at an elevation angle of about 45 degrees. The load data was taken for a comparable period, looking at the load. The spectrum has a

corresponds to a 3.5% transmission, or an isolation of 15dB, which is not ideal, but has little impact on small signals.

[12]The moon was determined to have an elevation of 33° at the time of this scan.

Figure 5.5: Plot of the Un-Demodulated Moon Scan

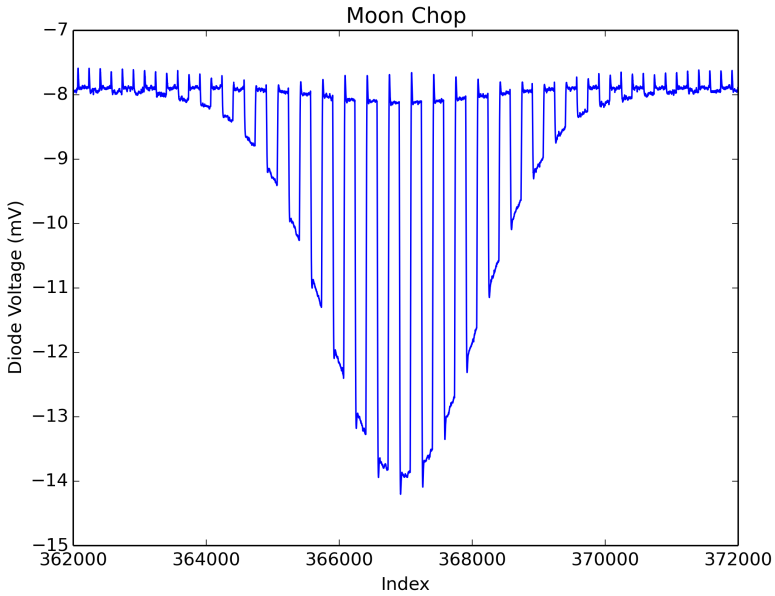

frequency resolution of $\sim$ 40mHz and is a clear $1/f$ slope below 10Hz. The spikes in the spectrum are due to RFI. Unfortunately this data was taken with the telescope oriented in a position where it picked up RFI.[13]

The load spectrum is similar to the except that the sky data has a large $1/f$ component that rises well above the load spectrum below 1Hz, but both of the spectra show a rise in the white noise level starting at about 10Hz. The large sky $1/f$ is likely due to variations in the sky temperature on timescales greater than 1 second. This variation makes it difficult to show the $1/f$ behavior of the amplifier itself. Still, it is possible to chop the data and remove some the $1/f$ component that is present in both the sky and load data.

The standard way to mitigate $1/f$ noise is to chop (using a front-end switch) the antenna signal with a thermal reference load (or another signal). The switch on the

[13]The presence of RFI is actually larger in the load data than in the sky data, suggesting that it is not just getting in through the front end, but may actually be coupling in some other way.

Figure 5.6: Log-Log Plot of Sky and Load PSD (Y-axis should read uV/BW)

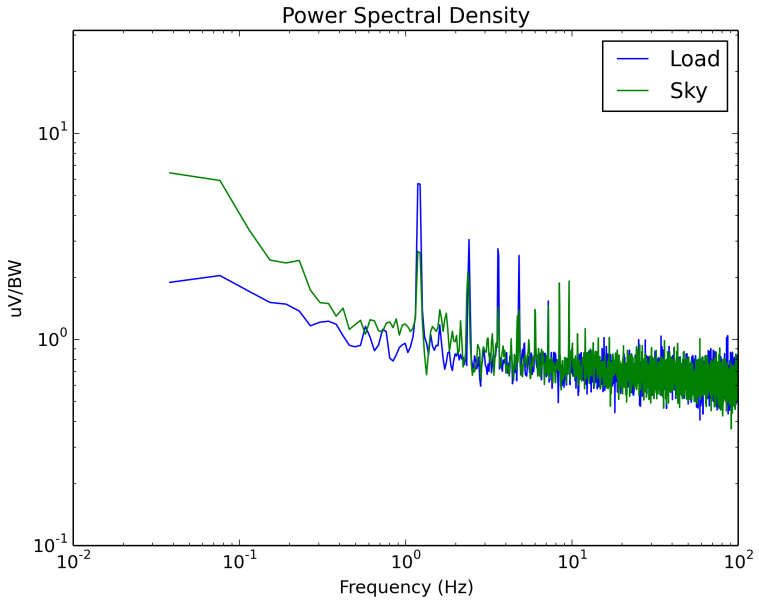

input to the amplifier consists of a transmission line with two PIN diodes to ground. When reverse biased, the diodes do nothing to the transmission line and the sky signal is transmitted to the amplifier. When the diodes are biased forward the diodes act as a short to ground, which reflects the sky signal back towards the horn. The noise out of the amplifier input is reflected back to the amplifier and acts as a load with a temperature very close to the amplifier noise temperature.

Figure 5.7 shows the PSD of a long dataset taken with the telescope in the configuration described above, but the with the switch cycling at 30Hz, so the highest frequency component is at 15Hz. The data is demodulated by taking the average of each half-cycle and subtracting it from the other half-cycle. The workhorse Python package used in the demodulation is Pandas[14], which gracefully handles database-style transformation. The go-to function (attribute) for much of the data processing was

[14]NumPy is the more fundamental Python data handler, but doesn't have the higher-level functionality of Pandas.

Figure 5.7: Log-Log Plot of Chopped Data PSD

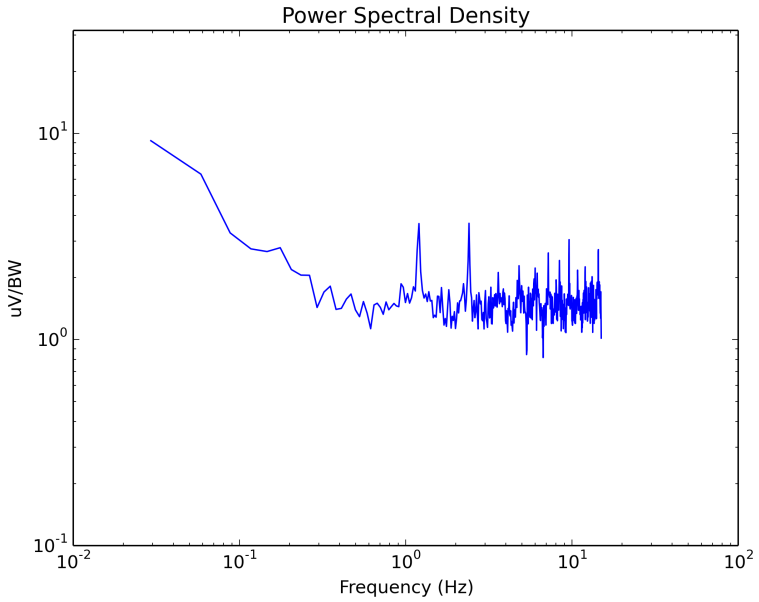

groupby(), which applies a given operation to groups in the data depending on the values in one or more chosen columns. The chopped data rate is 30Hz, but the integration time is at most a half-cycle period.[15]

The chop frequency is chosen to be 30Hz, above the frequency at which $1/f$ first detectable, but as low as possible to avoid loss of integration time. The first chopped data revealed a spike during the transition between the shorted and transmitting modes. This spike is cold, in the sense that the power dips significantly during the transition. It is hard to say what could cause power to be removed from the transmission line, even for a short period, but since it occurs when the switch changes states it is probably related to the transition between the forward and reverse bias behavior of the diodes.[16] This switching spike is clearly visible in the plot (Figure 5.8)

[15]This, combined with the fact that the chopped data is the difference between the two half-cycles increases the white noise level by a factor of two above data that is not chopped.

[16]The expectation is that a lossy partial short while the bias current is turning on would be at a temperature intermediate to the sky and amplifier input temperatures, but this is not the case.

Figure 5.8: Plot of switching spike (AC)

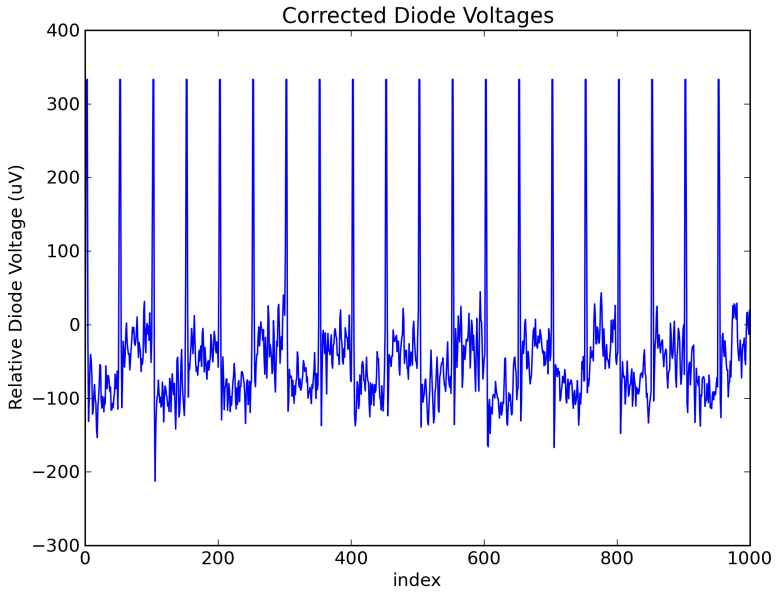

of the AC coupled diode output voltage. The chop rate in this plot is 100Hz. With the additional gain in the AC channel the spikes are out of the DAQ range and appear clipped in the data. Driving the DAQ beyond its measurement range could cause unreliable performance or damage, so it was necessary to reduce the spike amplitude by changing the integration constant before the AC gain stage from 3kHz to 300Hz.[17] The result is a broader but smaller amplitude spike that is well within the DAQ range.

Since lowering the low-pass filter roll off increases the spike width more data points have to be removed from each transition, so the amount of time on actual signal is reduced. To reduce the loss of data, the chop rate was reduced to 30Hz. The data in Figure 5.9 shows 1000 data point with 35 points removed from every transition to eliminate the spike.[18] The valid data points are stitched together in the

[17]It is unclear what the effect of railing the DAQ is exactly.
[18]The data rate is 10kHz, so each spike takes 3.5ms to subside in the filter.

Figure 5.9: Plot of Signal and Reference

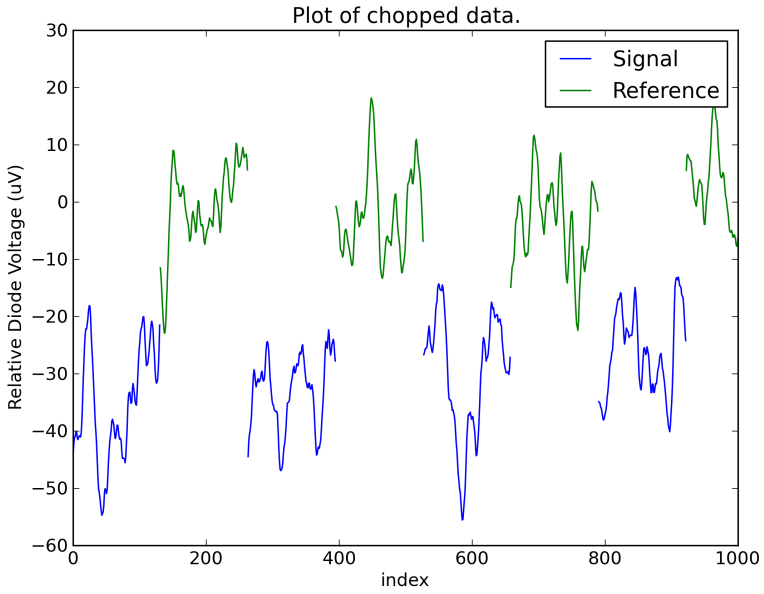

plot so 4 complete cycles appear.

The uncertainty in the demodulated data can be calculated given the number of samples that are averaged together in each cycle. This number is 131 or 132 (depending on the phase), corresponding to just 13ms. This time, multiplied by the receiver band-width of 500MHz, plugged into the radiometer equation gives a relative uncertainty of close to 4×10^{-4}. Taking the receiver temperature to be 20K, the expected temperature uncertainty of the raw demodulated output is about 7.84mK in each switch cycle. To calculate the temperature uncertainty given the time the telescope, it is useful to calculate the Dicke switch efficiency (called κ in the Noise chapter). This number is 2 for an ideal Dicke switch (using reference load), and 2.25 for this Dicke switch. Assuming zero offset temperature ($\Delta T = 0$) so that $1/f$ doesn't contribute at all, the expected temperature uncertainty for this receiver is $2\text{mK}/\sqrt{\text{s}}$.

5.3 Pseudo-Maps

The normal data-taking procedure is to record the switching radiometer output as the telescope rotates at a rate of about 1 revolution per minute in azimuth with a fixed elevation angle. This data is recorded synchronously with the a sync line that indicates the state of the switch and with the encoder outputs that indicate position. The raw data is then demodulated by a Python code that finds the average sky diode voltage relative to the load average voltage. This data is binned according to azimuth angle[19] so that it can be easily plotted.

The pseudo-maps are images formed by stacking the data from each rotation into an array of hight equal to the number of rotations and length 1800 azimuth bins, and plotting the array in a gray-scale image. The first such pseudo-map made is shown in figure 5.10. The vertical axis is rotation number, with the first rotation at the top, so the number label is actually backwards. There are nearly 200 rotations in this image, corresponding to about 3 hours of observation. The horizontal axis is azimuth angle measure West of North[20]. The azimuth position was estimated based on an old offset and turned out to be off by several degrees. The gray-scale is in units of relative microvolts out of the diode.

The first obvious feature in this image is the galaxy (this is verified later), which appears as a slanted pair of lines toward the left side. The orientation of the galactic plane is roughly North-South, so the point at which the telescope beam crosses it drifts towards the West as time progresses. There is a much smaller feature towards the lower right side of the image may also be of extra-terrestrial origin, but this hasn't been confirmed. There is a clear error in pointing that resulted in one scan across

[19] a standard $5 \times 360 = 1800$ bins are used for every telescope rotation, roughly corresponding to the data rate.

[20] Apparently the convention is to measure this angle East of North, the opposite of normal Cartesian angles and the encoder direction.

Figure 5.10: Image of Raw Pseudo-Map

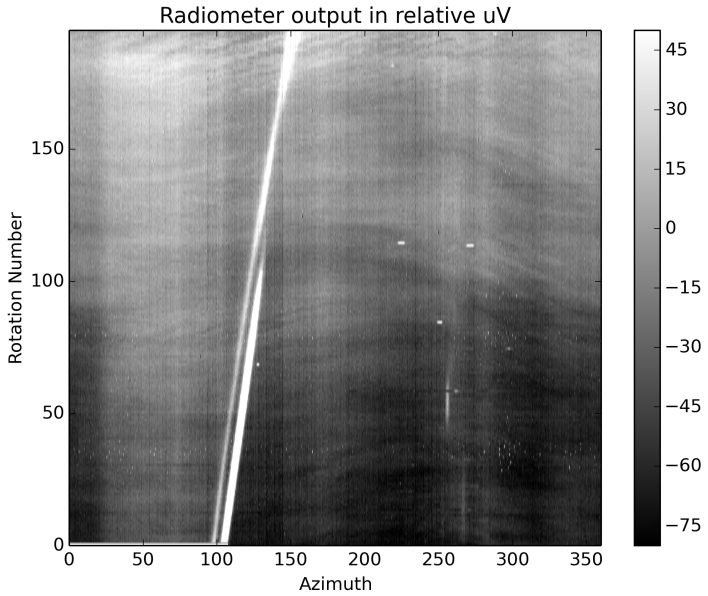

this object being shifted to the right.[21] The other noticeable feature is a relatively large-scale temperature fluctuation that seems to

There are several small bright features that are too narrow to have been scanned by the beam. These are undoubtedly due to transient RFI. The other obvious terrestrial signal in the image is a striping pattern that is correlated strongly with azimuth angle. These stripes may be due to side-lobe pickup from warm objects around the telescope, such as the elevator shaft to the North, or constant directional RFI in the form of in-band signal, or out-of-band compression.

Several corrections are made to the raw images. One image observes the moon for several rotations. The central scan of the moon was used (along with the time stamp) to correct the Azimuth position. An attempt was made to remove the RFI spikes by searching the data for pixels much brighter than those in adjacent rotations

[21]The encoder cable shield was accidentally left ungrounded during this data set and the encoder data had to be heavily cleaned to remove noise that coupled in from the large azimuth servo motor.

with the same azimuth angle, and removing them. The vertical stripes are difficult to remove entirely, but they are mitigated by subtracting the average (taken along the rotation axis) from every pixel with the same azimuth angle. The average (and the subtraction) exclude pixels with a brightness above some threshold in order to avoid over-subtraction. This approach is imperfect and leaves stripes where the edges of bright features are below the threshold.

Figure 5.11 show a cleaned map. The gray-scale is in units of milliKelvin (using a conversion ration of 4mK/μV), stretched from -200 to 275mK. With the azimuth striping removed, some of the rotation-axis striping becomes more visible. This process, despite making the map appear clearer, actually seems to make the tens of milliKelvin-scale fluctuations throughout the map less visible. These fluctuations have clear bands that stretch across a significant fraction of the sky, and pass through the beam over the course of several rotations. The pattern these fluctuations produce in the map resembles diurnal motion, but since the slope of their motion is different from that of the galactic plane it is clear that they are not extra-terrestrial in origin. The fluctuating bands are likely due to variations in the sky temperature, with a pattern that indicates a general westward airflow. These fluctuations are the limiting factor in measurements taken on the Santa Barbara sky, and extra-terrestrial signals smaller than a few tens of milliKelvin are obscured.

The bright features in the galactic plane are clipped to highlight limit of sensitivity in the data. The AC data has high gain such that features brighter than a couple of degrees are out of the range of the baseband amplifiers as well as the data acquisition system,[22] but the DC data has much less gain, and the range to record the full receiver output. The DC data shows that the brightest feature in this map has a

[22]Briefly railing the amps and DAQ is probably not damaging to the hardware, but the data points immediately following the railed data are suspect.

Figure 5.11: Image of Cleaned Pseudo-Map

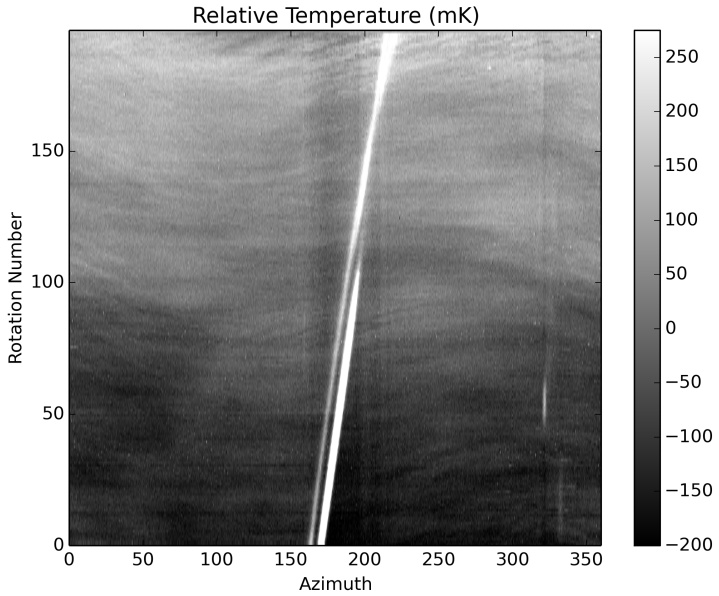

temperature of 18K. This source appears $\sim 1.5^\circ$ wide, and so was not immediately identified as the moon, but no other sources could be as bright. The fact that this source is (probably a glancing pass by) the moon is supported by ephemeris data.

Figure 5.12 was taken on the night of August 11 during a (mostly) full moon, at a lower elevation angle than the previous map. The moon is clearly visible to the right of the galaxy. The rotation that passes closest to the center of the moon was taken at 11:30 pm, when the moons elevation angle was about 33°.[23] The moon was also $\sim 75^\circ$ from the galactic center, located at about $\sim 28^\circ$ elevation. This puts the moon in about the right position in the map relative to the bright galactic plane.

More observations were taken on different nights, and at different elevation angles. The map in figure 5.13 was taken at an elevation angle so low that the beam clips the winch on top of the elevator shaft to the North, which could have been used to

[23]This value was found using PyEphem, a python wrapper on XEphem, and confirmed using NASA's Horizons ephemeris calculator.

Figure 5.12: Image of Pseudo-Map with the Moon

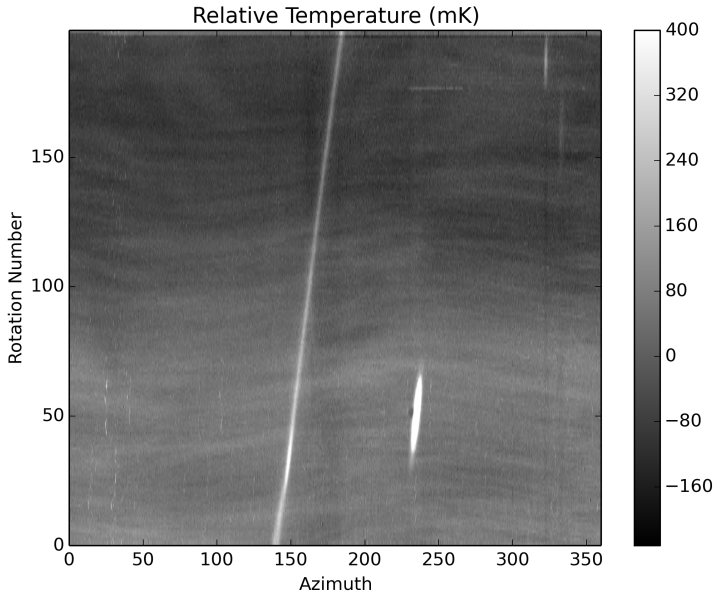

roughly align the pointing. The walls on either side of the elevator shaft itself are also visible. Figure 5.14 was taken earlier during the night of the full moon, and contain several bright features that were thought to be clouds. These features appear to drift through the map at a rate much greater than the galaxy, but the pattern is very odd (it does not correspond to a single wind direction). It is more likely that these features are due to a periodic RFI source, and the apparent motion due to the difference in the rotation rate and the period of the RFI.

5.4 Conclusions and Future Work

The uncertainty in the temperature measurements taken on some relatively clear evening skies above UC Santa Barbara during the Month of August is on the order of 10mK and the variations in the sky temperature are on the 100mK scale. There is good evidence that the amplifier $1/f$ noise is reduced by chopping, but since the

Figure 5.13: Image of Pseudo-Map with the Building

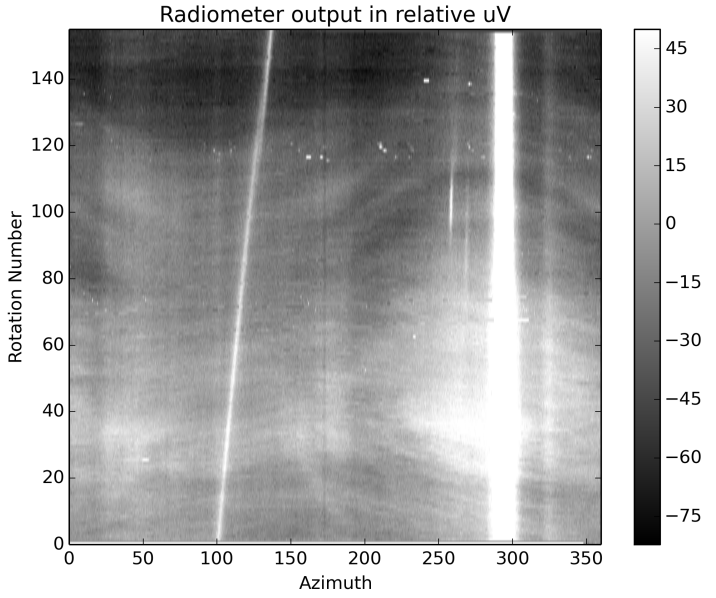

Figure 5.14: Image of Pseudo-Map with Clouds

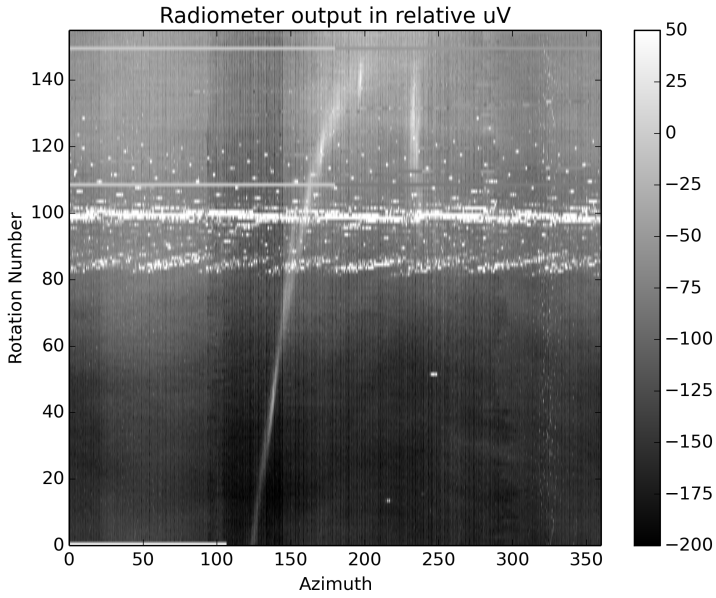

only available cold target at a temperature close to the cold load (the amplifier input noise) is the sky, with temperature variations of its own, it is not possible to determine the frequency of the demodulated $1/f$ knee is. The limited stability of the sky temperature places the upper limit at around 0.3Hz. The second brightest source observed after the moon was a point on the galactic plane near the center with a temperature of about 20K.

There are several limitations to chopping against a load of fixed temperature other than the limit on the $1/f$ measurement. There is a very real problem of balancing the receiver given a sky of lower temperature. The relatively low elevation angle at which the data above was taken was in part due to the need to find an elevation at which the sky temperature matched the load temperature. The variations in the sky temperature are presumably lower at higher elevation angle, but no data was taken above $\sim 40^{\circ}$ elevation. Another reason to take low elevation data is to maximize sky coverage, so clearer low elevation skies would be ideal.

At lower sky temperature, as would be expected at observation sites such as White Mountain, the load temperature would either have to be reduced to maintain a balanced load, or another approach should be taken. One way to balance the receiver would be to add noise power to the sky signal. This of course would increase the system uncertainty. The notion that a slightly unbalanced receiver could be tolerated if the full amplitude of the signal could be measured was introduced in the Noise chapter. The difficulty in measuring the full signal amplitude is due to the limited dynamic range of the analog electronics and of the data acquisition system. This could be overcome with a system that introduces a low-noise voltage to offset the DC component. Such a system was built, but never tested. In fact, data of this sort exists for all of the maps above. This data can be demodulated in exactly the same way as the AC data (that has passed through a high pass filter), but if the voltage

offset is known (this also exists in the data), it can be added back to the in-range signal to find the absolute gain for each switch cycle.

5.4.1 Future Work

The first avenue to explore with this instrument is to write demodulation code to analyze the absolute voltage data. If this demodulation works, the next step would be to take data in Santa Barbara at relatively high elevation angles to try to get a better measurement of the receiver $1/f$.

The next big issue with this instrument is that it is still susceptible to RFI. More RFI data taken with the new RFI blocking band-pass filters would help in understanding this problem. The real answer to RFI though, is simply to get away from it. Although it is impossible to get away from all RFI, it is expected that the site at white mountain would have significantly less RFI. RFI data should be taken at White Mountain to understand the challenge there.

As a final though, there is a way to mitigate variations in the temperature of the atmosphere, but it requires a different type of receiver. A Dicke switch that looks alternately at a horn that points in a given direction in the sky and another horn that points in a direction a couple of beam widths away could hope to eliminate some of the larger angular scale temperature variation. This type of receiver would require a SPDT switch, but is well worth the effort, as the actual observation time would double, and, the receiver would be automatically very well balanced at all times. If I were to build a new instrument, a receiver that chops between two horns would be my goal.

Bibliography

[1] A. Lazarian B.T. Draine. Electric dipole radiation from spinning dust grains. *The Astrophysical Journal*, 508(157–179), 1998.

[2] G. Hinshaw M. R. Nolta N. Odegard L. Page D. N. Spergel J. L. Weiland E. L. Wright M. Halpern N. Jarosik A. Kogut M. Limon S. S. Meyer G. S. Tucker E. Wollack C. Bennett, R. S. Hill. First year wilkinson microwave anisotropy probe (wmap) observations: Foreground emission. *The Astrophysical Journal*, June 2003.

[3] Gregory Dobler Dan Hooper, Douglas P. Finkbeiner. Evidence of dark matter annihilations in the wmap haze. *Physical Review*, D76, May 2007.

[4] Marc Davis David J. Schlegel, Douglas P. Finkbeiner. Maps of dust ir emission for use in estimation of reddening and cmbr foregrounds. *The Astrophysical Journal*, 500(525), 1998.

[5] R. H. Dicke. The measurement of thermal radtiation at microwave frequencies. *The review of scientific instruments*, 17(7):268–275, April 1946.

[6] Curtis Frank Carl Heiles Douglas P. Finkbeiner, David J. Schlegel. Tentative detection of electric dipole emission from rapidly rotating dust grains. *The Astrophysical Journal*, 566(898), 2002.

[7] M. W. Pospieszalski E. J. Wollack. Characteristics of broadband inp millimeter-wave amplifiers for radiometry. *IEEE MTT-S Digest*, (0-7803-4471-5/98):669–672, March 1998.

[8] Rodrigo Leonardi et al. The cosmic foreground explorer (cofe): A balloon-borne microwave polarimeter to characterize polarized foregrounds. *New Astrononmy Review*, 50:977–983, 2006.

[9] Douglas P. Finkbeiner. A full-sky h-alpha template for microwave foreground prediction. *The Astrophysical Journal Supplement Series*, 146, 2003.

[10] Douglas P. Finkbeiner. Microwave ism emission observed by wmap. *The Astrophysical Journal*, 614:186–193, December 2003.

[11] Douglas P. Finkbeiner. Wmap microwave emission interpreted as dark matter annihilation in the inner galaxy. *The Astrophysical Journal*, 614:186–193, January 2005.

[12] Robert H. Frater and David R. Williams. An active cold noise source. *IEEE Transaction on Microwave Theory and Techniques*, MTT-29(4), April 1981.

[13] C. L. Bennett R. Bean O. Dore M. R. Greason M. Halpern R. S. Hill N. Jarosik A. Kogut E. Komatsu M. Limon N. Odegard S. S. Meyer L. Page H. V. Peiris D. N. Spergel G. S. Tucker L. Verde J. L. Weiland E. Wollack G. Hinshaw, M. R. Nolta and E. L. Wright. Three-year wilkinson microwave anisotropy probe (wmap1) observations: Temperature analysis. *The Astrophysical Journal Supplement Series*, 170:288–334, June 2007.

[14] Douglas P. Finkbeiner Gregory Dobler. Extended anomalous foreground emission in the wmap 3-year data. *The Astrophysical Journal*, 680:1222–1234, 2008.

[15] J. I. Lee I. K. Han. Low frequency noise in hemt structure. *Journal of the Korean Physical Society*, 39:S322–S326, December 2001.

[16] John C. Kraus. *Radio Astronomy.* Cygnus-Quasar Books.

[17] C. L. Bennett N. Jarosik, C. Barnes. First year wilkinson microwave anisotropy probe (wmap) observations: On-orbit radiometer characterization. *The Astrophysical Journal Supplement Series*, 148(29), 2003.

[18] C.L. Bennett N. Jarosik. Design, implementation and testing of the map radiometers. *The Astrophysical Journal Supplement Series*, 2003.

[19] Boaz Porat. *A Course in Digital Signal Processing.* John Wiley & Sons, Inc., 1997.

[20] P. Meinhold P. Lubin T. Gaier, M. Seifert. Noise performance of a cryogenicaly cooled 94ghz inp mmic amplifier and radiometer. *SPIE*, 2842(8194-230-4):46–54, 1996.

[21] S. WEINREB. Cryogenic performance of microwave terminations, attenuators, absorbers, and coaxial cable. *ELECTRONICS DIVISION INTERNAL REPORT*, (223), January 1982.

[22] Brian Williams. *B-Machine Polarimeter: A Telescope to Measure the Polarization of the Cosmic Microwave Background.* PhD thesis, UCSB.